Smoothed Particle Hydrodynamics Implementation of the Standard Viscous-Plastic Sea-Ice Model and Validation in Simple Idealized Experiments

ORESTE MARQUIS, Atmospheric and Oceanic Sciences

McGill University, Montreal

AUGUST, 2022

A thesis submitted to McGill University in partial fulfillment of the requirements of the degree of

Master of Science

Table of Contents

List of Figures

List of Tables

List of Variables

Physical property

t   Simulation time

Δ Total deformation

η Shear viscosity

Γ 1D stress proportionality factor

λ Wavelength

$\dot{\epsilon}$ Strain rate tensor

σ Cauchy's stress tensor

τ Drag force

r   General position vector

u   Velocity vector

x   Ice position vector

ω Angular velocity

ζ Bulk viscosity

A Ice concentration

c Phase speed

h Mean ice thickness

k Wavenumber

m Mass

P Ice strength

S Ice shear strength

Smoothed Particle Hydrodynamics specifics

α A free parameter

κ Boundary force parameter

l Smoothing length

N Number of particles

R Normalize distance in the kernel referential

W SPH kernel function

Other symbols

δf A small element

δ_{ij} Dirac delta function

$\hat{\mathbf{x}}$ X direction unit vector

$\hat{\mathbf{y}}$ Y direction unit vector

$\mathbf{T}$ A given tensor

$\mathbf{V}$ A given vector

$\mathcal{A}$ An Area

$\mathcal{F}$ Fourier transform

$\mathcal{S}$ A Surface

$\mathcal{V}$ A Volume

f A given function

L A Length

Physics constants

ρ Material density

C Drag coefficient

C^* Ice strength decay

e Ellipse yield curve aspect ratio

k_t Tensile strength factor

P^* Ice compressive strength

Superscript

C Relative to a classical definition

n Relative to an iteration number

Subscript

0 Relative to unperturbed/initial value

A Relative to the concentration

a Relative to the air

b Relative to a boundary particle

d Relative to dimension

i Relative to the ice

max Relative to a maximum

min Relative to a minimum

p Relative to the current particle

q Relative to a neighbour particle

r Relative to a replacement

SPH Relative to the SPH Viscous-Plastic theory

TOT Relative to a total

VP Relative to the Viscous-Plastic theory

w Relative to the water

List of Acronyms

DEM Discrete-Element Method. 4, 5, 31, 33, 35, 37

EVP Elastic-Viscous-Plastic. 4, 34

FDM Finite-Difference Method. iv, xii, xiii, 4, 5, 22, 23, 25, 31, 35–38, 40

FEM Finite-Element Method. 4, 5, 35, 38

FVM Finite-Volume Method. 4, 5

GCM Global Climate Model. 39

LKFs Linear Kinematic Features. 4, 5, 39

MIZ Marginal Ice Zone. 27–29, 37

SPH Smoothed Particle Hydrodynamics. iii, iv, xii–xiv, 8–10, 13–16, 20, 22, 23, 25, 26, 28, 31, 32, 34–40

VP Viscous-Plastic. iv, xii, xiii, 4–7, 13, 20, 23, 25, 36

Abstract

The Viscous-Plastic (VP) rheology with an elliptical yield curve and normal flow rule is implemented in a Lagrangian modelling framework using the Smoothed Particle Hydrodynamics (SPH) meshfree method. Results show, from perturbation analysis of SPH sea-ice dynamic equations, that the classical SPH particle density formulation expressed as a function of sea-ice concentration and mean ice thickness, leads to incorrect plastic wave speed. We propose a new formulation for particle density that gives a plastic wave speed in line with theory. In all cases, the plastic wave in the SPH framework is dispersive and depends on the smoothing length (i.e., the spatial resolution) and on the SPH kernel employed in contrast with its finite difference method (FDM) implementation counterpart. The steady-state solution for the simple 1D ridging experiment is in agreement with the analytical solution within an error of 1%. SPH is also able to simulate a stable upstream ice arch in an idealized domain representing the Nares Strait in low wind regime (5.3 $[\mathrm{m} \cdot \mathrm{s}^{-1}]$) with an ellipse aspect ratio of 2, an average thickness of 1 $[\mathrm{m}]$ and free-slip boundary conditions in opposition to the FDM implementation that requires higher shear strength to simulate it. In higher wind regime (7.5 $[\mathrm{m} \cdot \mathrm{s}^{-1}]$) no stable ice arches are simulated — unless the thickness is increased — and the ice arch formation showed no dependence on the size of particles contrary to what is observed in the discrete element framework. Finally, the SPH framework is explicit, can take full advantage of parallel processing capabilities and show potential for pan-arctic climate simulations.

Abrégé

La rhéologie visqueuse-plastique (VP) avec une courbe de rendement elliptique et une règle d'écoulement normale est mise en œuvre dans un cadre de modélisation Lagrangien en utilisant la méthode sans maillage de l'hydrodynamique des particules lissées (SPH). Les résultats montrent, à partir d'une analyse des perturbations des équations SPH de la dynamique de la glace de mer, que la formulation classique de la densité des particules SPH exprimée en fonction de la concentration de la glace de mer et de l'épaisseur moyenne de la glace conduit à une vitesse incorrecte des ondes plastiques. Nous proposons une nouvelle formulation pour la densité de particules qui donne une vitesse d'onde plastique conforme à la théorie. Dans tous les cas, l'onde plastique dans le cadre SPH est dispersive et dépend de la longueur de lissage (c'est-à-dire de la résolution spatiale) et du noyau SPH employé, contrairement à des modèles homologues basés sur la méthode des différences finies (FDM). La solution à l'état stationnaire pour l'expérience simple de crête 1D est en accord avec la solution analytique avec une erreur de 1%. Le SPH est également capable de simuler une arche de glace stable en amont dans un domaine idéalisé représentant le détroit de Nares pour un régime de vent faible (5,3 $[\mathrm{m} \cdot \mathrm{s}^{-1}]$) avec un rapport d'aspect d'ellipse de 2, une épaisseur moyenne de 1 $[\mathrm{m}]$ et des conditions limites de glissement libre, contrairement à l'implémentation FDM qui nécessite une force de cisaillement plus élevée pour la simuler. Dans un régime de vent plus élevé (7,5 $[\mathrm{m} \cdot \mathrm{s}^{-1}]$), aucune arche de glace stable n'est simulée — à moins que l'épaisseur ne soit augmentée — et la formation d'arches de glace ne montre aucune dépendance à la taille des particules, contrairement à ce qui est observé dans le cadre des éléments discrets.

Enfin, le cadre SPH est explicite, peut tirer pleinement parti des capacités de traitement parallèle et présente un potentiel pour les simulations climatiques panarctiques.

Acknowledgements

Chapter 1

Foreword

This Master's Thesis will be adapted to a paper that will be submitted to The Cryosphere journal in the early fall of 2022. All of the required elements for a thesis are included: an introduction with a comprehensive review of the relevant literature, a model description section, research findings with a comprehensive scholarly discussion and a conclusion. The FORTRAN SPH sea-ice model code was developed from scratch by Oreste Marquis and is now public. It can be found at https://github.com/McGill-sea-ice/SIMP. Output data from the SPH sea-ice model along with a version of the model used, simulations presented in the thesis and the analyzing programs are available at https://10.5281/zenodo.6950156.

1.1   Manuscript Information

Title: Smoothed Particle Hydrodynamics Implementation of the Standard Viscous-Plastic Sea-Ice Model and Validation in Simple Idealized Experiments
Authors: Oreste Marquis, Bruno Tremblay, Jean-François Lemieux and Mohammed (Shameem) Islam
To be submitted to: The Cryosphere

1.2   Author and Co-authors Contributions

Oreste Marquis designed, developed and coded the model. Oreste Marquis carried out the literature review, ran all the simulations, analyzed the results with the supervision and suggestion of Bruno Tremblay. The writing was done in collaboration between Bruno Tremblay and Oreste Marquis, with comments from Jean-Francois Lemieux and Mohammed (Shameem) Islam.

Chapter 2

Introduction

Sea-ice plays an important role in climate (Budikova, 2009). It modulates the radiative fluxes at the surface and influence the atmospheric energy balance (Gardner, Sharp, 2010; Södergren et al., 2017). It insulates the relatively warm ocean from the atmosphere because of its low thermal conductivity and reduces the vertical heat and moisture fluxes affecting mesoscale atmospheric processes (Maykut, 1982; Kottmeier, Engelbart, 1992; Haid, Timmermann, 2013; Dethleff, 2013). Sea-ice modifies the seasonal cycle of temperature because of the latent heat released when freezing and absorbed when melting (Walsh, 1983; Fichefet, Maqueda, 1997). It influence the ocean circulation (Aagaard et al., 1981; Ohshima et al., 2016) and deep-water formation (Smith et al., 1990; Maqueda, 2004) when frazil crystals form and brine is rejected in one location and freshwater released in another. The vertical mixing and convection induced by this ice formation and melting also brings nutrient-rich benthic water that supports biological productivity and wildlife (Stirling, 1980, 1997; Arrigo, 2004; Kalenitchenko et al., 2019).

For accurate climate projection of the Earth's system a sea-ice component must be included. Numerical models for geophysical sea-ice have historically employed a continuum approach where the material is discretized on an Eulerian mesh using various constitutive relations. For example, the standard Viscous-Plastic model (Hibler, 1979) or

modifications (e.g., Elastic-Viscous-Plastic or EVP and Elastic-Plastic-Anisotropic or EPA Hunke, Dukowicz, 1997; Tsamados et al., 2013), solves a set of partial differential equations using the finite-difference method (FDM). FDM is the simplest method to discretize and solve partial differential equations numerically. However, it is based on a local Taylor series expansion to approximate the continuum equations and construct a topologically rectangular network of relations between nodes (e.g., Arakawa grids).

Even though the VP (and EVP) rheologies are commonly used to describe sea-ice dynamics and are able to capture important large-scale deformation features (Bouchat et al., 2022; Hutter et al., 2022), they still have difficulties to represent smaller scale properties (Schulson, 2004; Weiss et al., 2007; Coon et al., 2007) such as Linear Kinematic Features (LKFs) unless run at very high resolution (≈ 2 km, Ringeisen et al., 2019; Hutter et al., 2022). To improve the simulation of small-scale ice features and to alleviate the problem of FDM with complex geometries (Peiró, Sherwin, 2005), the community also considered new sea-ice rheologies (Schreyer et al., 2006; Girard et al., 2011; Dansereau et al., 2016; Ringeisen et al., 2019) and explored different space discretization frameworks like the finite-element method (FEM) (Rampal et al., 2016; Mehlmann et al., 2021), the finite-volume method (FVM) (Losch et al., 2010; Adcroft et al., 2019) or the discrete-element method (DEM) (Hopkins, Thorndike, 2006; Herman, 2016; Damsgaard et al., 2018).

In recent decades, spatial resolution of sea-ice models became comparable to the characteristic length of the ice floes. This makes the continuum assumption of current FDM, FVM and FEM models questionable. Also, Eulerian models are known to have difficulties determining the precise locations of inhomogeneity, free surfaces, deformable boundaries and moving interfaces (Liu, Liu, 2010). These shortcomings have led to an increase interest in the DEM approach. Another advantage of using DEM is that granularity of the material (Overland et al., 1998) is directly represented using discrete rigid bodies from which the physical interactions are calculated explicitly in the hope that larger scale properties

4

naturally emerge. In practice, the emergent properties still depend on the assumed floe size and the nature of collisions. Nevertheless, DEM easily captures formation of cracks, leads and large deformation making it a consistent framework for the numerical simulation of granular material like sea-ice (Fleissner et al., 2007).

Despite the shortcomings of the continuum approaches, FDM, FVM and FEM are still the most commonly used framework in the community because they have been developed and tested for a longer period, they are well understood, more computationally efficient and easily coupled for synoptic scale simulations. In an attempt to take advantages of both continuum and discrete formulation, blends between the two approaches have been proposed — e.g., the finite-discrete element (Lilja et al., 2021) or the material-point method (Sulsky et al., 2007). Those framework, however, still use a mesh to solve the dynamic equations in addition to considering sea ice as discrete elements making them even more computationally expensive. Finally, a fairly new approach for sea-ice modelling — also taking from both continuum and discrete framework — uses a Lagrangian meshfree continuous method called smoothed particle hydrodynamics (SPH) (Lucy, 1977; Gingold, Monaghan, 1977). This meshfree method is known to facilitates the numerical treatment and description of free surfaces (Liu, Liu, 2010) which are common in sea-ice dynamics with polynyas, LKFs, free drifting ice floes and unbounded ice extent. As in DEM, the physical quantities are carried out by particles in space (an analogy for ice floes in the real world), but evolve according to the same dynamic equations used in the continuum approach. Furthermore, the method has the advantage of treating the system of equations in a Lagrangian framework discretized explicitly making it well suited for parallelization.

SPH has been used successfully for the modelling of other granular materials such as sand, gravels and soils (Salehizadeh, Shafiei, 2019; Yang et al., 2020; Sheikh et al., 2020). In the context of mesoscale and larger sea-ice modelling, Gutfraind, Savage (1997) initiated the SPH study of sea-ice dynamics using a VP rheology based on a Mohr-Coulomb

failure criterion. The ice concentration and thickness were fixed at 100% and 1 [m] with a continuity equation expressed in terms of a particle density. The internal ice strength between particle was derived diagnostically from ice density assuming ice was a nearly incompressible material. Later, Wang (2000) developed a sea ice model of the Bohai Sea (east coast of China) using an SPH viscous-plastic rheology (Hibler, 1979) with continuity equations for ice concentration and mean thickness, and ice strength calculated from static ice jam theory (Shen et al., 1990). Following Wang (2000), Ji et al. (2005) implemented a new viscoelastic-plastic rheology that was in better agreement with observations from the Bohai Sea. Recently, Staroszczyk (2017) proposed a sea ice model considering ice to behave as a compressible non-linear viscous material with a (dimensionless) contact length dependent parameterization for floe collisions and rafting (Gray, Morland, 1994; Morland, Staroszczyk, 1998). In all of the above, except for Gutfraind, Savage (1997), the same ice particle density definition is used.

In this work, we use the standard VP sea-ice model with an elliptical yield curve and normal flow rule (Hibler, 1979), and propose a reformulation of the ice particle density that is internally consistent with the model physics. One goal of the study is to investigate differences coming from the numerical framework. To this end, we theoretically investigate the plastic wave propagation, a fundamental property of a sea-ice physical model, throughout a 1D perturbations analysis and we test the model in a ridging and ice arch experiment following earlier works by Lipscomb et al. (2007); Dumont et al. (2009); Rabatel et al. (2015); Dansereau et al. (2017); Williams et al. (2017); Damsgaard et al. (2018); Ranta et al. (2018); Plante et al. (2020); West et al. (2022). We chose to investigate the SPH method performance on a ridging experiment since it has an analytical steady-state solution that can be used to establish the model accuracy and it is possible to evaluate the coherent evolution of the continuity equations. We also test SPH performance on ice arches simulation since this classic problem is an example of large-scale features resulting from small-scale interaction involving fractures of the material. The two experiments al-

6

low a direct comparison with previous work and identify advantages and disadvantages with the continuum and discrete sea-ice dynamic. The long-term goal is to lay the foundation for an SPH sea-ice formulation that can be used in synoptic scale models.

The thesis is organized as follows. In chapter 3, the SPH framework and how the sea-ice VP rheology, momentum and continuity equations can be implemented in this framework are described. Results of a plastic wave propagation analysis, ridging experiments, and ice-arching simulations are presented in the chapter 4. Finally, chapter 5 discuss the SPH advantages and limitations of the framework and model developed and concludes.

Chapter 3

Model

3.1 Smoothed Particle Hydrodynamics (SPH)

The SPH method is at the interface between finite element method and discrete element methods. In this framework any function $f(\mathbf{r})$ at a point $\mathbf{r}$ is approximated from neighbouring values in the parameter space $f(\mathbf{r}')$ using an integral interpolant (see figure 3.1):

$$f(\mathbf{r}) = \int_{\mathcal{V}} f(\mathbf{r}') W(|\mathbf{r} - \mathbf{r}'|, l) d\mathbf{r}', \tag{3.1}$$

where $W(|\mathbf{r} - \mathbf{r}'|, l)$ is the interpolating kernel and $\mathcal{V}$ is the entire space volume. In two dimensions, the space volume is an area $\mathcal{A}$ and the kernel has units of $[\mathrm{m}^{-2}]$. This integral interpolant approximation is based on the singular integral mathematical framework of Natanson (1961) and imposes the following restrictions on the kernel:

$$\int_{\mathcal{A}} W(|\mathbf{r} - \mathbf{r}'|, l) d\mathbf{r}' = 1, \tag{3.2}$$

and

$$\lim_{l \to 0} W(|\mathbf{r} - \mathbf{r}'|, l) = \delta(\mathbf{r} - \mathbf{r}'), \tag{3.3}$$
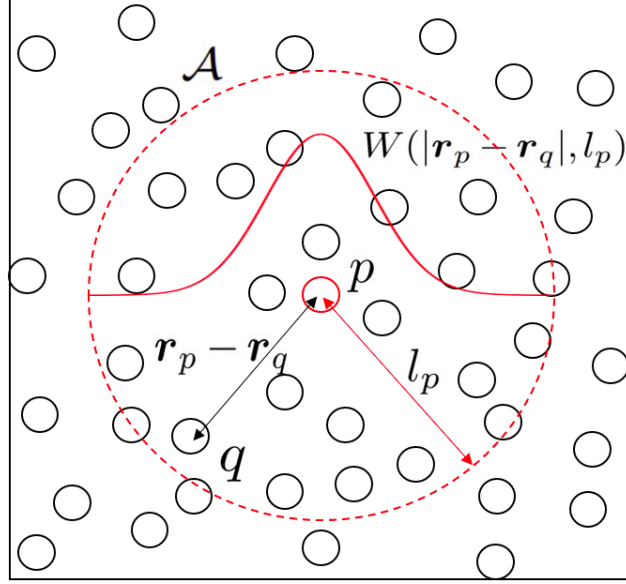
Figure 3.1: Graphical representation of the SPH kernel $W(|\mathbf{r}_p - \mathbf{r}_q|, l_p)$ (solid red line), the smoothing length l_p (red arrow), the particle p, the neighbouring particles q, the support domain $\mathcal{A}$ (dashed red line) and the distance between any neighbour particle q and the particle p within the support domain $\mathbf{r}_p - \mathbf{r}_q$ (black arrow). Note that particles are points in space and that their size in this schematic is arbitrary.

where l is the smoothing length of the kernel and δ is the Dirac delta function. Using the particle approximation, Eq. (3.1) can be written as a weighted summation over all neighbouring points within the area $\mathcal{A}$:

$$f(\mathbf{r}_p) \approx \sum_{q=1}^{N} f(\mathbf{r}_q)W(|\mathbf{r}_p - \mathbf{r}_q|, l_p)\Delta\mathcal{A}_q \approx \sum_{q=1}^{N} f(\mathbf{r}_q)W(|\mathbf{r}_p - \mathbf{r}_q|, l_p)\frac{m_q}{\rho_q}, \qquad (3.4)$$

where N is the number of points in space referred as neighbour particles, $\Delta\mathcal{A}_q$ $(= m/\rho)$ is the area associated with the particle p, m represent the mass [kg] and ρ is the 2D density [$\mathrm{kg} \cdot \mathrm{m}^{-2}$]. From the above approximations, we reformulate differential operators relevant to our study in their discrete SPH forms. We write the divergence of a vector field (**V**), the divergence of a tensor (**T**) and the gradient of a vector field (**V**) (Monaghan, 2005) as

(see Appendix 6.1 for complete derivation) :

$$(\nabla \cdot \mathbf{V})_p = \frac{1}{\rho_p} \sum_{q=1}^{N} m_q (\mathbf{V}(\mathbf{r}_q) - \mathbf{V}(\mathbf{r}_p)) \cdot \nabla_p W_{pq}, \tag{3.5}$$

$$(\nabla \cdot \mathbf{T})_p = \rho_p \sum_{q=1}^{N} m_q \left(\frac{\mathbf{T}(\mathbf{r}_q)}{\rho_q^2} + \frac{\mathbf{T}(\mathbf{r}_p)}{\rho_p^2} \right) \cdot \nabla_p W_{pq}, \tag{3.6}$$

$$(\nabla \mathbf{V})_p = \sum_{q=1}^{N} \frac{m_q}{\rho_q} (\mathbf{V}(\mathbf{r}_q) - \mathbf{V}(\mathbf{r}_p)) \otimes \nabla_p W_{pq}. \tag{3.7}$$

In Eq. (3.7), $\otimes$ denotes the outer product. $\nabla_p W_{pq}$ is the gradient of the kernel at the coordinate $\mathbf{r}_p - \mathbf{r}_q$ in the reference frame of particle p and is written as :

$$\nabla_p W_{pq} = \frac{\mathbf{r}_p - \mathbf{r}_q}{|\mathbf{r}_p - \mathbf{r}_q|} \frac{\partial W(|\mathbf{r}_p - \mathbf{r}_q|, l_p)}{\partial |\mathbf{r}_p - \mathbf{r}_q|}. \tag{3.8}$$

Note that W_{pq} is a scalar function and consequently $\nabla_p W_{pq}$ is a vector, the inner product in Eq. (3.5) is a scalar, the inner product in Eq. (3.6) is a 2D vector and the outer product in Eq. (3.7) is a 2D tensor of rank 2. In addition to Eq. (3.2 - 3.3), the smoothing kernel must have the following set of properties to avoid non-physical behaviour and costly computation (Liu, Liu, 2003):

Compact support : $\qquad\qquad W(|\mathbf{r}_p - \mathbf{r}_q|, l_p) = 0$, for $|\mathbf{r}_p - \mathbf{r}_q| > l_p$, $\qquad$ (3.9)

Positive definite : $\qquad\qquad W(|\mathbf{r}_p - \mathbf{r}_q|, l_p) \geq 0$, $\qquad\qquad\qquad\qquad$ (3.10)

Monotonically decreasing : $\dfrac{\partial W(|\mathbf{r}_p - \mathbf{r}_q|, l_p)}{\partial (|\mathbf{r}_p - \mathbf{r}_q|)} \leq 0$, $\qquad\qquad\qquad$ (3.11)

Symmetric : $\qquad\qquad W(|\mathbf{r}_p - \mathbf{r}_q|, l_p) = W(-|\mathbf{r}_p - \mathbf{r}_q|, l_p)$, $\qquad$ (3.12)

Differentiable : $\qquad\qquad \dfrac{\partial^n W(|\mathbf{r}_p - \mathbf{r}_q|, l_p)}{\partial (|\mathbf{r}_p - \mathbf{r}_q|)^n} \exists$, $\qquad\qquad\qquad$ (3.13)

where $\exists$ stands for *exist*. In the above, differentiable means that the kernel derivatives exist up to the highest order present in the equations. Finally, to ensure the consistency of the SPH method approximations to the nth order, all kernel moments of order 1 to n

need to vanish. In practice, the consistency conditions are satisfied when the number of neighbouring particles is sufficiently large to be evenly distributed in the domain of influence (Fraga Filho, 2019). Note that, at the boundaries, the domain of influence of the particle is truncated making it impossible to satisfy the kernel moments equations. This phenomenon is referred as the particle inconsistency and leads to poorer approximations of physical properties. No clear solutions to this problem are proposed in the literature yet.

3.2 Momentum and continuity equations

Following Plante et al. (2020), we consider sea-ice to behave as a two-dimensional granular material described by the 2D momentum equation (neglecting the Coriolis and sea surface tilt terms):

$$\rho_i h \frac{\mathrm{D}\mathbf{u}}{\mathrm{D}t} = \nabla \cdot \sigma + \tau, \tag{3.14}$$

where ρ_i is the ice density, h is the mean ice thickness (ice volume over an area), $\mathbf{u} = u\hat{\mathbf{x}} + v\hat{\mathbf{y}}$ is the ice velocity vector, σ is the vertically integrated internal stress tensor acting in the $\hat{\mathbf{y}}$ direction on a face with a unit outward normal pointing in the $\hat{\mathbf{x}}$ direction, τ is the sum of water drag and surface air stress and $\frac{\mathrm{D}}{\mathrm{D}t} = \frac{\partial}{\partial t} + \mathbf{u} \cdot \nabla$ is the Lagrangian derivative operator. We neglected the Coriolis and sea surface tilt force in the momentum equation to make it easier to validate the model and study the ice arch formation. Note that using the Lagrangian derivative operator naturally incorporates the advection of momentum in the ice dynamics — a term that is typically neglected for most continuum based Eulerian sea-ice models. The surface air stress and the water stress can be written using bulk formulation as (McPhee, 1979):

$$\tau = \rho_a C_a |\mathbf{u}_a - \mathbf{u}|(\mathbf{u}_a - \mathbf{u}) + \rho_w C_w |\mathbf{u}_w - \mathbf{u}|(\mathbf{u}_w - \mathbf{u}), \tag{3.15}$$

$$\approx \rho_a C_a |\mathbf{u}_a|(\mathbf{u}_a) + \rho_w C_w |\mathbf{u}_w - \mathbf{u}|(\mathbf{u}_w - \mathbf{u}), \tag{3.16}$$

where ρ_a and ρ_w are air and water densities, $\mathbf{u}_a$ and $\mathbf{u}_w$ are air and water velocity vectors, C_a and C_w are the air and water drag coefficients and where $\mathbf{u}$ is neglected in the formulation of the wind stress since $\mathbf{u} \ll \mathbf{u}_a$. The continuity equations for the mean ice thickness h and the ice concentration A can be written as:

$$\frac{\mathrm{D}h}{\mathrm{D}t} + h\nabla \cdot \mathbf{u} = 0, \tag{3.17}$$

$$\frac{\mathrm{D}A}{\mathrm{D}t} + A\nabla \cdot \mathbf{u} = 0, \tag{3.18}$$

where the thermodynamic source terms are omitted.

3.3 Constitutive laws

The constitutive relations for the viscous-plastic ice model with an elliptical yield curve, a normal flow rule and tensile strength can be written as (Beatty, Holland, 2010):

$$\sigma_{ij} = 2\eta\dot{\epsilon}_{ij} + \left[(\zeta - \eta)\dot{\epsilon}_{kk} - \frac{P_r(1 - k_t)}{2}\right]\delta_{ij}, \tag{3.19}$$

$$\dot{\epsilon}_{ij} = \frac{1}{2}\left(\frac{\partial u_j}{\partial x_i} + \frac{\partial u_i}{\partial x_j}\right) = \frac{1}{2}\left(\nabla\mathbf{u} + \nabla\mathbf{u}^\intercal\right), \tag{3.20}$$

where $\dot{\epsilon}_{ij}$ is the symmetric part of the strain-rate tensor, ζ and η are the non-linear bulk and shear viscosities, P_r is the replacement pressure, k_t is the tensile strength factor and δ_{ij} is the Kronecker delta. Following Bouchat, Tremblay (2017) we write :

$$\zeta = \frac{P(1 + k_t)}{2\Delta^*}, \tag{3.21}$$

$$\eta = \frac{\zeta}{e^2} = \zeta\left(\frac{2S}{P(1 + k_t)}\right)^2, \tag{3.22}$$

$$\Delta^* = \max(\Delta, \Delta_{min}), \tag{3.23}$$

$$\Delta = \left[(\dot{\epsilon}_{11}^2 + \dot{\epsilon}_{22}^2)(1 + e^{-2}) + 4e^{-2}\dot{\epsilon}_{12}^2 + 2\dot{\epsilon}_{11}\dot{\epsilon}_{22}(1 - e^{-2})\right]^{1/2}, \tag{3.24}$$

where $P = P^*h \exp(-C(1-A))$ is the ice strength (Hibler, 1979), P^* and C are respectively the ice compressive strength and ice concentration parameters, S is the ice shear strength and e is the ellipse aspect ratio. In the limit where the strain rates $\dot{\epsilon}$ go to zero, ζ and η would tend to infinity. To avoid this situation, the deformation Δ is capped to $\Delta_{min} = 2 \times 10^{-9}\text{s}^{-1}$. Using the Δ^* formulation, the replacement pressure P_r can be written as

$$P_r = P\frac{\Delta}{\Delta^*}, \tag{3.25}$$

which ensures that the stresses are zero when the strain rates are zero.

3.4   Governing differential equations: SPH framework

To solve ice dynamic system of equations in the SPH framework, equations involving spatial derivatives (Eqs. 3.14 - 3.17 - 3.18 - 3.20) are reformulated using Eqs. (3.5 - 3.6 - 3.7) with the particle subscripts p and q (see Fig. 3.1) and a temporal evolution for the ice particle position is defined:

$$\frac{\mathrm{D}\mathbf{x}_p}{\mathrm{D}t} = \mathbf{u}_p, \tag{3.26}$$

$$\rho_i h_p \frac{\mathrm{D}\mathbf{u}_p}{\mathrm{D}t} = \rho_p \sum_{q=1}^{N} m_q \left(\frac{\sigma_q}{\rho_q^2} + \frac{\sigma_p}{\rho_p^2} \right) \cdot \nabla_p W_{pq} + \tau_p, \tag{3.27}$$

$$\frac{\mathrm{D}h_p}{\mathrm{D}t} + \frac{h_p}{\rho_p} \sum_{q=1}^{N} m_q (\mathbf{u}_q - \mathbf{u}_p) \cdot \nabla_p W_{pq} = 0, \tag{3.28}$$

$$\frac{\mathrm{D}A_p}{\mathrm{D}t} + \frac{A_p}{\rho_p} \sum_{q=1}^{N} m_q (\mathbf{u}_q - \mathbf{u}_p) \cdot \nabla_p W_{pq} = 0, \tag{3.29}$$

$$(\dot{\epsilon}_{ij})_p = \frac{1}{2} \left[\left(\sum_{q=1}^{N} \frac{m_q}{\rho_q} (\mathbf{u}_q - \mathbf{u}_p) \otimes \nabla_p W_{pq} \right) + \left(\sum_{q=1}^{N} \frac{m_q}{\rho_q} (\mathbf{u}_q - \mathbf{u}_p) \otimes \nabla_p W_{pq} \right)^{\mathsf{T}} \right]. \tag{3.30}$$

It is important to make the distinction between the intrinsic ice density ρ_i and the particle densities ρ_p. For consistency reasons with the standard VP rheology, we consider the following definition of density independent of ice concentration in contrast with previous

work (Wang, 2000; Ji et al., 2005; Staroszczyk, 2017) (see results section for discussion):

$$\rho_p = \rho_i h_p. \tag{3.31}$$

By formulating density as Eq. (3.31), the continuity Eq. (3.28) has the same form as the more commonly used continuity density equation (Monaghan, 2012) :

$$\frac{\mathrm{D}\rho_p}{\mathrm{D}t} = -\rho_p \nabla \cdot \mathbf{u}_p = \sum_{q=1}^{N} m_q (\mathbf{u}_p - \mathbf{u}_q) \cdot \nabla_p W_{pq}, \tag{3.32}$$

except for the fact that the divergence of the velocity field is scaled by the ice material density ρ_i ($\frac{\mathrm{D}\rho_p}{\mathrm{D}t} = \rho_i \frac{\mathrm{D}h_p}{\mathrm{D}t}$). Note that since the particle density ρ_p is independent of the concentration, the particle concentration A_p is a quantity that measures the compactness of the floes at the particle location, but does not relate to the amount of ice carried by a particle. With this formulation, the concentration can be interpreted as the probability of ice floes carried by a particle to come in contact with ice floes of another particle (and repel each other) within the unresolved area ΔA_p.

3.5 Numerical approach

Following Hosseini et al. (2019), we use a second order predictor-corrector scheme to evolve in time the SPH ice system of equation (see algorithm 1 below). This integration scheme takes a given function f (here f can be $\mathbf{x}$, $\mathbf{u}$, A and h) and used a predictor step to calculate its value $f^{n+1/2}$ at time $t = (n + \frac{1}{2})\Delta t$ (where Δt is the time step) followed by a correction step to calculate the solution f^{n+1} at time $t = (n + 1)\Delta t$ from $f^{n+1/2}$:

$$f_p^{n+1/2} = f_p^n + \frac{\Delta t}{2}\frac{\mathrm{D}f_p^n}{\mathrm{D}t} + O(\Delta t^2), \tag{3.33}$$

$$f_{p\,\text{corrected}}^{n+1/2} = f_p^n + \frac{\Delta t}{2}\frac{\mathrm{D}f_p^{n+1/2}}{\mathrm{D}t}, \tag{3.34}$$

$$f_p^{n+1} = 2f_{p\,\text{corrected}}^{n+1/2} - f_p^n + O(\Delta t^3). \tag{3.35}$$

Following Lemieux, Tremblay (2009), a simple 1D model taking into account only the viscous term — the most restrictive condition — leads to the following stability criterion:

$$\Delta t \leq \frac{\rho_i h l_{min}^2}{\eta_{max}} = \frac{e^2 \rho_i l_{min}^2 \Delta_{min}}{P^*(1 + k_t)}, \tag{3.36}$$

where l_{min} is the minimum smoothing length across all the particles.

Algorithm 1 Sea-ice SPH

Require: Domain shape and boundaries, Spatial resolution, Total integration time
    initialize particle and boundary according to input
    for $i = 0$ **to** $IntegrationTime$ **do**
        $nInteraction \leftarrow nearestNeighbourParticleSearch$
        for $j = 0$ **to** $nInteraction$ **do**
            $kernel \leftarrow smoothingFunctionCalculation$
            $internalForce \leftarrow kernel$
        end for
        for all $particles$ **do**
            $externalForce$
            $physicalQuantities \leftarrow (externalForce, internalForce)$
            $density \leftarrow iceThickness$
            $smoothingLength \leftarrow density$
        end for
        $timeStep \leftarrow smoothingLength$
        monitor particle interaction statistics
        output
    end for

3.6   Particle interactions

Following Rhoades (1992), we use the bucket search algorithm parallelized using shared memory multiprocessing (OpenMP) to find all the neighbours of each particle in favour of the explored tree algorithm (Cavelan et al., 2019) which involve pointers and complex memory structure that are not easy to manipulate in OpenMP.

After the neighbour search, the interactions between pairs of particles are computed us-

ing the Wendland C^6 kernel — Wendland kernels have the best stability properties for wavelengths smaller than the smoothing kernel (Dehnen, Aly, 2012) — which is written as:

$$W(|\mathbf{r}_p - \mathbf{r}_q|, l_p) \quad = W_{C^6}(R) \quad = \alpha_d \begin{cases} (1-R)^8(32R^3 + 25R^2 + 8R + 1), & 0 \leq R < 1, \\ 0, & R \geq 1, \end{cases}$$

$$(3.37)$$

$$\frac{\partial W(|\mathbf{r}_p - \mathbf{r}_q|, l_p)}{\partial |\mathbf{r}_q - \mathbf{r}_p|} = \frac{\partial W_{C^6}(R)}{\partial |\mathbf{r}_q - \mathbf{r}_p|} = \alpha_d \begin{cases} -22R(16R^2 + 7R + 1)(1-R)^7\frac{\kappa}{l_p}, & 0 \leq R < 1, \\ 0, & R \geq 1, \end{cases}$$

$$(3.38)$$

where α_d is a normalization factor depending on the dimension of the problem. Note that $R \ (= \kappa|\mathbf{r}_p - \mathbf{r}_q|/l_p)$ is the normalized distance between particles in the referential $\mathbf{r}_p - \mathbf{r}_q$. Consequently, we always integrate from 0 to l_p (the smoothing length) independently of the kernel instead of 0 to κl_p as shown in (Liu, Liu, 2010). The constant α_d becomes $\frac{78\kappa^2}{7\pi l^2}$ in 2D, with a factor of κ^2 different from the usual definition. Note that the scaling factor κ has a value of 1 for the Wendland C^6 kernel. The choice of kernel was validated using stability tests with six different kernels including the original Gaussian kernel (Gingold, Monaghan, 1977), a quartic spline Gaussian approximation (Liu, Liu, 2010), a quintic spline Gaussian approximation (Morris et al., 1997), a quadratic kernel (Johnson, Beissel, 1996) and the Wendland C^2, C^4 and C^6 kernels (Wendland, 1995).

3.7   Smoothing length

The smoothing or correlation length is a key element of SPH and has a direct influence on the accuracy of the solution and the efficiency of the computation. For instance, if l_p is too small, there may not be enough particles in the support domain violating the kernel moments requirements. If the smoothing length l_p is too large, all the local properties

of particles would be smoothed out over large number of neighbours and the computation time would increase with the number interactions. In two dimensions the optimal number of neighbours interacting with any particle p should be about 20 to balance the precision and the computational cost (Liu, Liu, 2003). We therefore implement a variable smoothing length that evolves in time and space to maintain this approximate number of neighbours. To this end, we keep the mass of particles constant in time and evaluate the smoothing length from the particle density. Note that keeping the mass of a particle constant has the advantage of ensuring mass conservation. This assumption is justified in our case since we are only interested in sea-ice dynamics and ridging change the area cover by ice floes but not their mass. However, fixing the ice mass is only valid when neglecting the thermodynamics and need to be modified for synoptic scale simulation.

The initial mass of a particle is defined from the ice area it represents within its support domain ($\Delta \mathcal{A}_p$ in Fig. 3.2). To avoid creating porosity in the medium, we divide the space in equal square area ($= L_p^2$) that covers the whole domain. Since we want approximately 20 neighbours for every particle, we introduce α ($= 3$ in all simulations) a parameter that stands for the approximate number of particles desired in any direction within the support domain. The parameter α can also be interpreted as the proportionality constant between the particle spacing L_p and the smoothing length l_p. Note that to increase accuracy of the particle approximation, α can be increased by any desired factor (see Fig. 3.2). The mass carried by a particle is therefore written as :

$$m_p = \mathcal{A}_p \rho_i h_{0p} = L_p^2 \rho_i h_{0p}, \tag{3.39}$$

where h_{0p} is the initial mean thickness of the particle. The smoothing length is then updated at each time step diagnostically from:

$$l_p = \alpha L_p = \alpha \sqrt{\frac{m_p}{\rho_p}}. \tag{3.40}$$

The smoothing length l_p is capped to 10 times its initial value when the particle density
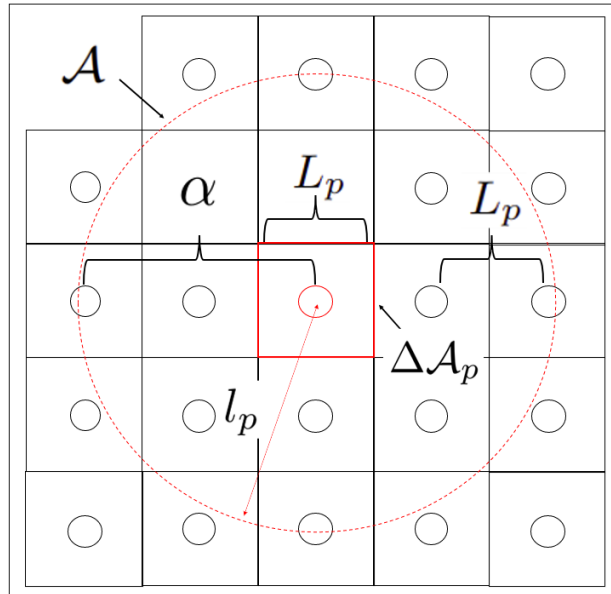
Figure 3.2: Graphical representation of the initial position of the particles and the relevant parameter for the smoothing length evolution : the ice area carried by the particle $\mathcal{A}_p$ (solid red square), the parameter α (= 2 in this schematic for visibility), the support domain $\mathcal{A}$ (dashed red line), the smoothing length l_p (red arrow) and the initial distance between particle L_p. Black circles are neighbouring particle q and the red circle is the current particle p. Note that, as for the figure 3.1, the particle sizes in this schematic are also arbitrary.

tends to zero. This capping prevents conservation of mass for density lower than 1% of its initial value (see Eq. (3.39)). We justify this capping because such small densities do not affect the ice dynamics.

3.8   Boundary treatment

We implemented the boundary treatment of Monaghan, Kajtar (2009) because of its simplicity, versatility and low computational cost. The boundaries are set up by placing stationary particles with fixed smoothing length l_b and a mass m_b equal to the average ice particle mass m_p. The boundary smoothing length l_b is chosen in a way that only one

layer of ice particles initially interact with the boundary (this makes l_b resolution dependent). The boundary particles are (equally) spaced apart by a factor one quarter of their smoothing length ($l_b/4$). In this manner, all ice particles p within a support domain l_b will interact with approximately four boundary particles (denoted by the subscript b) at a time resulting in a net normal repulsive force $\mathbf{F}_{\mathbf{N}p}$:

$$\mathbf{F}_{\mathbf{N}p} = \sum_{b=1}^{N_b} \kappa_n \frac{(\mathbf{r}_p - \mathbf{r}_b)}{|\mathbf{r}_p - \mathbf{r}_b|^2} W_{pb} \frac{2m_b}{m_p + m_b}, \tag{3.41}$$

that is added to their momentum equation. In Eq. (3.41), κ_n is a constant with units of [$\text{kg} \cdot \text{m}^4 \cdot \text{s}^{-2}$] used to adjust the repulsion strength and is also simulation dependent because it needs to counterbalance the particle acceleration, and prevent them from escaping the domain. This free parameter is not suited for complex pan-arctic simulations, but is sufficient in our idealize experiment study. A free-slip boundary condition in all simulations, i.e., no tangential friction force between boundary particle and ice particle is applied.

Table 3.1: Physical parameters used across all simulations

Parameter	Symbol	Value	Unit
Ice concentration parameter	C	20	-
Ice compressive strength parameter	P^*	27.5	$\text{kN} \cdot \text{m}^{-2}$
Air density	ρ_a	1.3	$\text{kg} \cdot \text{m}^{-3}$
Water density	ρ_w	1026	$\text{kg} \cdot \text{m}^{-3}$
Ice density	ρ_i	900	$\text{kg} \cdot \text{m}^{-3}$
Wind drag coefficient	C_a	1.2×10^{-3}	-
Water drag coefficient	C_w	5.5×10^{-3}	-
Minimal total deformation	Δ_{min}	2×10^{-9}	s^{-1}

[1] Values of the parameter used for the simulations are the same as the one presented in Williams et al. (2017) to facilitate comparison in the results section.

Chapter 4

Results and Discussion

4.1 Plastic wave propagation

We first compare the plastic wave speed for the VP dynamic equations with and without the SPH approximations. To this end, we do a perturbation analysis for a one-dimensional case with a fixed sea-ice concentration ($A = 1$). In this case, the 1D SPH sea-ice dynamic equations (Eqs. 3.26 - 3.29) form a system of three equations and three unknowns (x, u and h):

$$\frac{\mathrm{D}x_p}{\mathrm{D}t} = u_p \tag{4.1}$$

$$\frac{\mathrm{D}u_p}{\mathrm{D}t} = \Gamma \sum_{q=1}^{N} \frac{m_q}{\rho_i^2}\left(\frac{1}{h_q} + \frac{1}{h_p}\right)\frac{x_{pq}}{|x_{pq}|}\frac{\partial W}{\partial x_{pq}} + \tau_p, \tag{4.2}$$

$$\frac{\mathrm{D}h_p}{\mathrm{D}t} = -\frac{1}{\rho_i}\sum_{q=1}^{N} m_q(u_q - u_p)\frac{x_{pq}}{|x_{pq}|}\frac{\partial W}{\partial x_{pq}}, \tag{4.3}$$

where x_{pq} is a short form for $x_p - x_q$ and $\Gamma = \frac{P^*}{2}\left[\pm(e^{-2} + 1)^{1/2} - 1\right]$. In the above, we made use of the following 1D normal stress for convergent plastic motion (see Gray, 1999; Williams et al., 2017, for 1D normal stress derivation):

$$\sigma = \sigma_{xx} = \frac{P^*}{2}\left[\pm(e^{-2} + 1)^{1/2} - 1\right]h = \Gamma h. \tag{4.4}$$

Linearizing around a mean state ($\bar{u} = 0$ and $\bar{h} = h_0$), considering small perturbations (δx, δu and δh) and ignoring 2nd order term, we obtain:

$$\frac{\mathrm{D}\delta x_p}{\mathrm{D}t} = \delta u_p \tag{4.5}$$

$$\frac{\mathrm{D}\delta u_p}{\mathrm{D}t} = \frac{\Gamma}{\rho_i} \sum_{q=1}^{N} \Delta\mathcal{A}_q \frac{\bar{x}_{pq}}{|\bar{x}_{pq}|} \left(\frac{-1}{h_0}(\delta h_q + \delta h_p)\frac{\partial W}{\partial \bar{x}_{pq}} + 2(\delta x_p - \delta x_q)\frac{\partial^2 W}{\partial \bar{x}_{pq}^2} \right), \tag{4.6}$$

$$\frac{\mathrm{D}\delta h_p}{\mathrm{D}t} = -h_0 \sum_{q=1}^{N} \Delta\mathcal{A}_q \frac{\bar{x}_{pq}}{|\bar{x}_{pq}|}(\delta u_q - \delta u_p)\frac{\partial W}{\partial \bar{x}_{pq}}, \tag{4.7}$$

where $\Delta\mathcal{A}_q = \frac{m_q}{\rho_i h_0} = \frac{m_q}{\rho_q}$ (Eq. 3.4) and where we have used the binomial expansion $\frac{1}{h} = \frac{1}{h_0 + \delta h} \approx \frac{1}{h_0}(1 - \frac{\delta h}{h_0})$. Assuming perturbations have a wavelike solution of the form $\delta f = \hat{f} \exp(i(k\bar{x} - \omega t))$ — where i is the imaginary number, k is the wavenumber and ω is the angular velocity — the set of equations in the reference frame following the ice motion reduces to:

$$\hat{x} = \frac{i}{\omega}\hat{u}, \tag{4.8}$$

$$\hat{u} = \frac{i\Gamma}{\omega\rho_i} \sum_{q=1}^{N} \mathcal{A}_q \frac{\bar{x}_{pq}}{|\bar{x}_{pq}|} \left(\left[-\frac{\hat{h}}{h_0}(1 + \exp(-ik\bar{x}_{pq})) \right]\frac{\partial W}{\partial \bar{x}_{pq}} + 2\hat{x}(1 - \exp(-ik\bar{x}_{pq}))\frac{\partial^2 W_{pq}}{\partial \bar{x}_{pq}^2} \right), \tag{4.9}$$

$$\hat{h} = -\frac{ih_0\hat{u}}{\omega} \sum_{q=1}^{N} \mathcal{A}_q \frac{\bar{x}_{pq}}{|\bar{x}_{pq}|}(\exp(-ik\bar{x}_{pq}) - 1). \tag{4.10}$$

Note that since the ice is initially at rest, the Lagrangian and the Eulerian frameworks are equivalent. For large enough wavelength (so that the perturbation can be resolved across multiple particles with high accuracy i.e., $\lambda \geq l_p$ and $N \rightarrow \infty$), the summations can be written as integrals, i.e., $\sum_{q=1}^{N} \mathcal{A}_q \frac{\bar{x}_{pq}}{|\bar{x}_{pq}|}$ becomes $\int_{-\infty}^{\infty} \mathrm{d}\bar{x}_{pq}$. Taking advantage of the kernel

properties — i.e., all moments higher than 0 vanish — we can write Eqs. 4.9 - 4.10 as:

$$\hat{u} = \frac{-i\Gamma}{\omega\rho_i} \int_{-\infty}^{\infty} \left(\frac{\hat{h}}{h_0} \frac{\partial W}{\partial \bar{x}_{pq}} + 2\hat{x} \frac{\partial^2 W_{pq}}{\partial \bar{x}_{pq}^2} \right) \exp(-ik\bar{x}_{pq}) \mathrm{d}\bar{x}_{pq} = \frac{\Gamma}{\omega\rho_i} \left(\frac{\hat{h}}{h_0} k + i2k^2\hat{x} \right) \tilde{W}, \quad (4.11)$$

$$\hat{h} = -\frac{ih_0\hat{u}}{\omega} \int_{-\infty}^{\infty} \exp(-ik\bar{x}_{pq}) \frac{\partial W}{\partial \bar{x}_{pq}} \mathrm{d}\bar{x}_{pq} = \frac{h_0\hat{u}k}{\omega} \tilde{W}, \quad (4.12)$$

where the integrals have been converted to Fourier transform using $\mathcal{F}(\frac{\partial W}{\partial \bar{x}_{pq}}) = ik\mathcal{F}(W) = ik\tilde{W}$. Finally, combining Eqs. (4.8 - 4.11 - 4.12), the phase speed for the plastic wave ($\frac{\omega}{k}$) can be written as:

$$c_{\text{SPH}} = \frac{\omega}{k} = \pm\tilde{W}\sqrt{-\frac{\Gamma}{\rho_i}\left(\frac{2}{\tilde{W}} - 1\right)}. \quad (4.13)$$

For wavelengths much larger than the smoothing length ($\lambda \propto \frac{1}{k} \gg l_p$), the Fourier transform of the kernel tends to 1 ($\tilde{W} \approx 1$) and the SPH formulation reduces to the Viscous-Plastic theory without SPH approximations (see for instance Williams et al., 2017), i.e.:

$$c_{\text{VP}} = \pm\sqrt{-\frac{\Gamma}{\rho_i}}, \quad (4.14)$$

with a plastic wave propagation speed $c_{\text{VP}} \approx 5.7 \, [\text{m} \cdot \text{s}^{-1}]$ for typical sea-ice parameters (see Table 3.1). Consequently, a major difference of SPH with the FDM framework is that the plastic wave speed is dispersive with a phase velocity c_{SPH} that is dependent on the wavelength and the smoothing length. In general, only the plastic waves with a wavelength between approximately 1 and 11 times the smoothing length will have their travelling speed modified by more than 1%. More specifically, in the limit where the wavelength λ approaches the smoothing length l_p, the plastic wave speed increases in the SPH framework for a maximum value of $\approx 6.7 \, [\text{m} \cdot \text{s}^{-1}]$ (see Fig. 4.1 panel a). Note that for wavelength smaller than the smoothing length, the summations in Eqs. (4.11- 4.12) cannot be written as integrals but the particles still respond partially to the perturbations. This sometimes leads to the tensile and the zero-energy modes instabilities (Swegle et al., 1995). As mentioned above, Dehnen, Aly (2012) showed that Wendland kernels, can diminish the tensile instability and the pairing of particles. A deeper analysis of unresolved

waves ($\lambda < l_p$) in the context of sea-ice SPH dynamic equations is beyond the scope of the current study.

For the more general case when the base state allows for a variable concentration (linearized around a mean state $\bar{A} = A_0$) and considering the classical — denoted by a superscript C — particle density definition ($\rho_p^C = \rho_i h_p A_p$) used by Wang (2000); Ji et al. (2005); Staroszczyk (2017), the plastic wave speed becomes:

$$c_{\text{A,SPH}}^C = \pm\tilde{W}\sqrt{-\frac{\Gamma^*}{\rho_i}\left(CA_0 - 3 + \frac{2}{\tilde{W}}\right)}, \qquad (4.15)$$

where $\Gamma^* = \Gamma \exp(-C(1-A_0))$. We argue that the plastic wave speed $c_{\text{A,SPH}}^C$ obtained with the classical density definition does not converge (see Fig. 4.1 panel b) to the Viscous-Plastic theory, $c_{\text{A,VP}}$, derived from FDM (see Williams et al., 2017, for derivation):

$$c_{\text{A,VP}} = \pm\sqrt{-\frac{\Gamma^*}{\rho_i}\left(CA_0 + 1\right)}, \qquad (4.16)$$

because the ice concentration is taken into account in both the definition of ρ_p^C and implicitly in the definition of the average thickness h_p. When we consider the new formulation of particle density independent of concentration as proposed above (Eq. 3.31) the wave speed equation becomes:

$$c_{\text{A,SPH}} = \pm\tilde{W}\sqrt{-\frac{\Gamma^*}{\rho_i}\left(CA_0 - 1 + \frac{2}{\tilde{W}}\right)}, \qquad (4.17)$$

which reduces to the FDM VP theory (Eq. 4.16) when the wavelength is large compared to the smoothing length (see Fig. 4.1 panel c). However, the classical density definition is not wrong, Wang (2000); Ji et al. (2005); Staroszczyk (2017) used different formulation of the continuity equation in their model which makes our perturbation analysis only valid in the current study. In a similar manner as for the plastic wave speed with a fixed

concentration (Eq. 4.13), the wave speed $c_{\mathrm{A,SPH}}$ (Eq. 4.17) is dispersive and the wavelength between 1 and 11 times the smoothing length are those that are mostly affected (more than 1%). However, in this case, the plastic wave speed is damped for wavelengths close to the smoothing length for mean concentration state higher than 0.1. Note that while the plastic wave speed is defined for all A, it does not have a physical meaning for $A < 0.85$ since there are negligible ice-ice interactions.
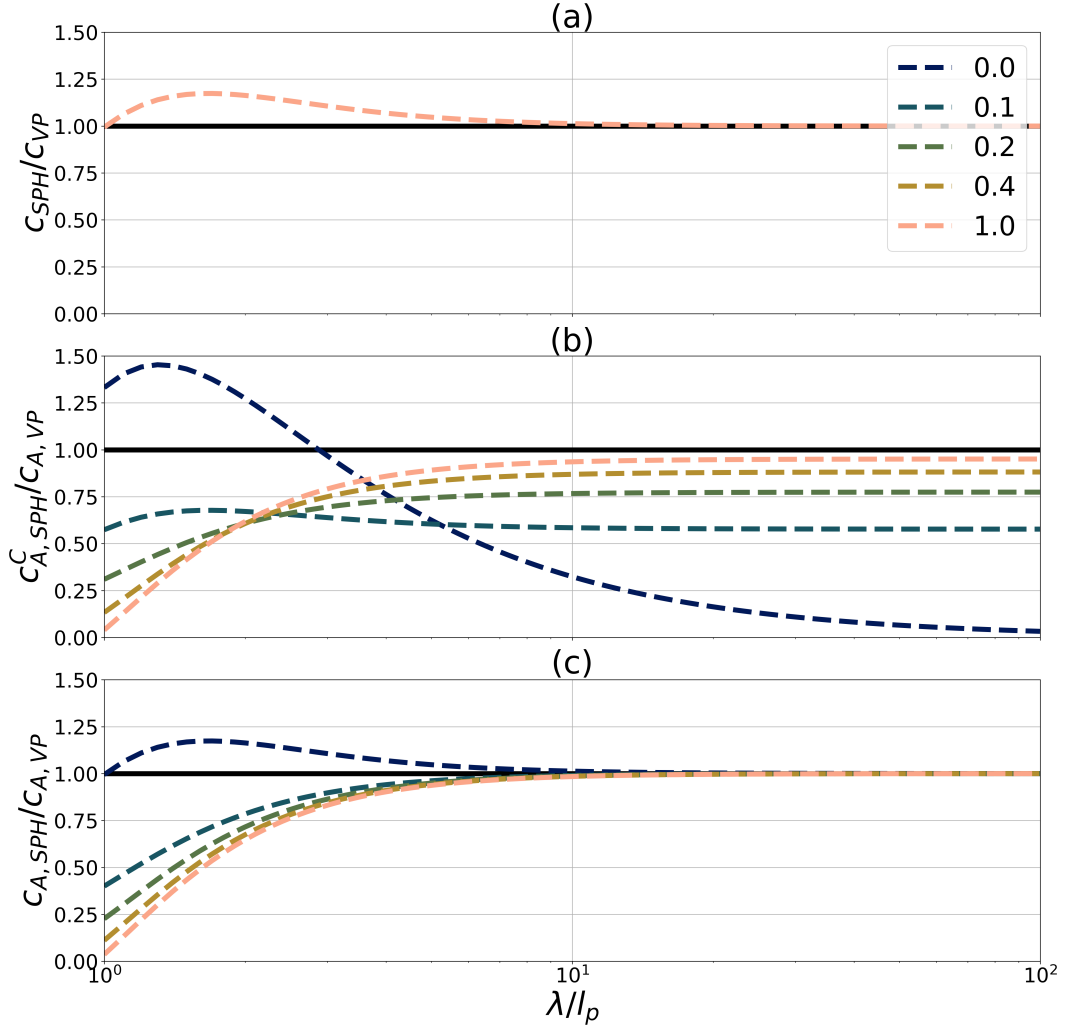
Figure 4.1: SPH plastic wave speed as a function of the normalized wavelength (λ/l_p) for the Wendland C^6 kernel. Panel a) show the classical VP rheology with fixed concentration (Eq. 4.13) normalized by the FDM plastic wave speed with fixed concentration (Eq. 4.14), panel b) show the classical VP rheology with a variable concentration and the density definition $\rho_p^C = \rho_i h_p A_p$ (Eq. 4.15) normalized by the FDM plastic wave speed with a variable concentration (Eq. 4.16) and panel c) show the classical VP rheology with a variable concentration and the density definition $\rho_p = \rho_i h_p$ (Eq. 4.17) normalized by the FDM plastic wave speed with a variable concentration (Eq. 4.16). Different homogeneous base state of concentration A_0 are shown varying from 0 to 1.

4.2 Ridging experiments

We validate our implementation of the SPH model (with the new definition of particle density ρ_p) in a 1D ridging experiment for which we have an analytical solution (see Williams, Tremblay, 2018, for derivation):

$$-\frac{\mathrm{d}\sigma}{\mathrm{d}x} = \rho_a C_a |u_a| u_a \implies \frac{\mathrm{d}h}{\mathrm{d}x} = \frac{2\rho_a C_a |u_a| u_a}{P^*(\sqrt{e^{-2}+1}+1)}, \tag{4.18}$$

i.e., a linear profile in thickness with a slope proportional to the square of the wind velocity and inversely proportional to the ice strength. We consider a rectangular domain of 1000 by 2000 [km] including the boundary (the ice field is 1900 [km] to ensure that no particle escape on the open side) with 37240 particles, an initial homogeneous smoothing length l_p of 21.429 [km] (spacing l_p/α = 7.14 [km]) and a smaller — to limit boundary effect — boundary particle smoothing length l_b of 4 [km] (spacing $l_b/4$ = 1.0 [km]) to represent the wall (see Fig. 4.2). Particles are initialized with an average thickness $h = 1$ [m] and a concentration $A = 1$. They are forced against the wall by a constant unidirectional wind of 5 [m $\cdot$ s^{-1}]. Note that the water drag force is removed in the simulation for a faster convergence to the steady state which enables higher resolution — a water current of 0 [m $\cdot$ s^{-1}] would slow down the ice and the ridge formation since it is driven by the advection speed. The Coriolis force should normally also have to be considered with this domain size and classical polar latitude — the Rossby number is $\mathcal{O}(10^{-2})$ —, but is neglected in this idealized experiment to conserve the symmetry of the solution and compare it to the theoretical 1D equation (Eq. 4.18). In results presented below (Fig. 4.3 - 4.4), the particles properties are averaged over a grid of approximately 10 by 5 [km] cells for plotting purposes. Results show that the simulated thickness field converges to the analytical solution (within an error of $\approx$ 1%) after $\approx$ 5 days with a slope of 1.33×10^{-3} [m $\cdot$ km^{-1}], compared with 1.34×10^{-3} [m $\cdot$ km^{-1}] for the theory. Artifacts are observed close to the boundary where the repulsive force prevent the particle from reaching the "wall". Additionally, when a particle comes into contact with the boundary with a cer-
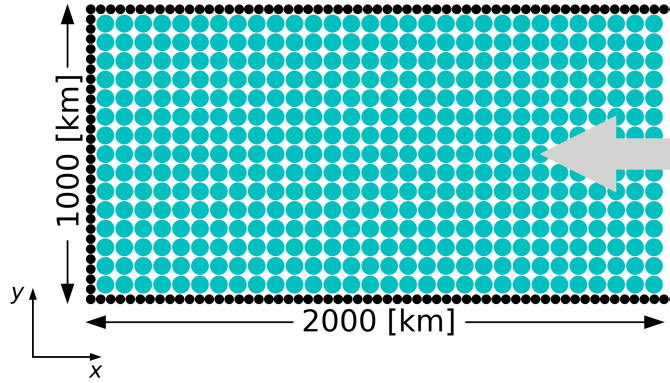
Figure 4.2: Idealized domain of the ridging experiment. The blue circles represent the ice particles and the black ones are the boundary particles. The grey arrow shows the wind forcing.

tain inertia (due to the $1/\mathbf{r}$ dependence of the boundary force), we observe oscillations in the motion of particles which can propagate far in the domain (e.g., Fig. 4.3 panel a, at $x \approx [50, 300]$ [km] and $t = [30, 45]$ [h]). The oscillations are damped and the energy is dissipated by the rheology term with time until an equilibrium is reached. A more physical boundary treatment is beyond the scope of this study.

We also tested the ridge formation in a concentration regime that transitions from 0.5 to 1 with the same forcing conditions and total sea-ice volume as before, i.e., an initial average thickness $h = 0.5$ [m] and an initial concentration $A = 0.5$ (see Fig. 4.3 panel b). To this end, the domain including the boundaries was extended in the $\hat{\mathbf{x}}$ direction to 4000 [km] (for a total ice field extent of 3800 [km]) and the initial particles spacing is changed from 7.14 [km] to 10.0 [km] with a corresponding initial smoothing length l_p of 30.0 [km] and a total number of particles of 38000. First, results show that the model converges in ≈ 10 days to a slope 1.36×10^{-3} [m $\cdot$ km^{-1}], which is also in agreement with theory within an error of $\approx 1\%$ (see Fig. 4.3 panel b). A noticeable difference with the simulation initialized at $A = 1$ is an average thickness greater than 1 building up outside of the ridge in the marginal ice zone (MIZ). This is because when a particle reaches a maximum concen-

tration before its neighbour, it will start ridging, but will not be able to move far from its current location because of the pressure applied by the surrounding particles resulting in a local increase of thickness. This local ridging stabilize at a thickness of approximately 1.1 [m] and is akin to the wave radiation drag in the MIZ (Sutherland, Dumont, 2018), even though no wave parametrization is implemented in the model. Further experimentation of convergent ice flow in the MIZ with concentration close to 1 will be considered in future work to explore this phenomenon. In order to test the behaviour of the continu-
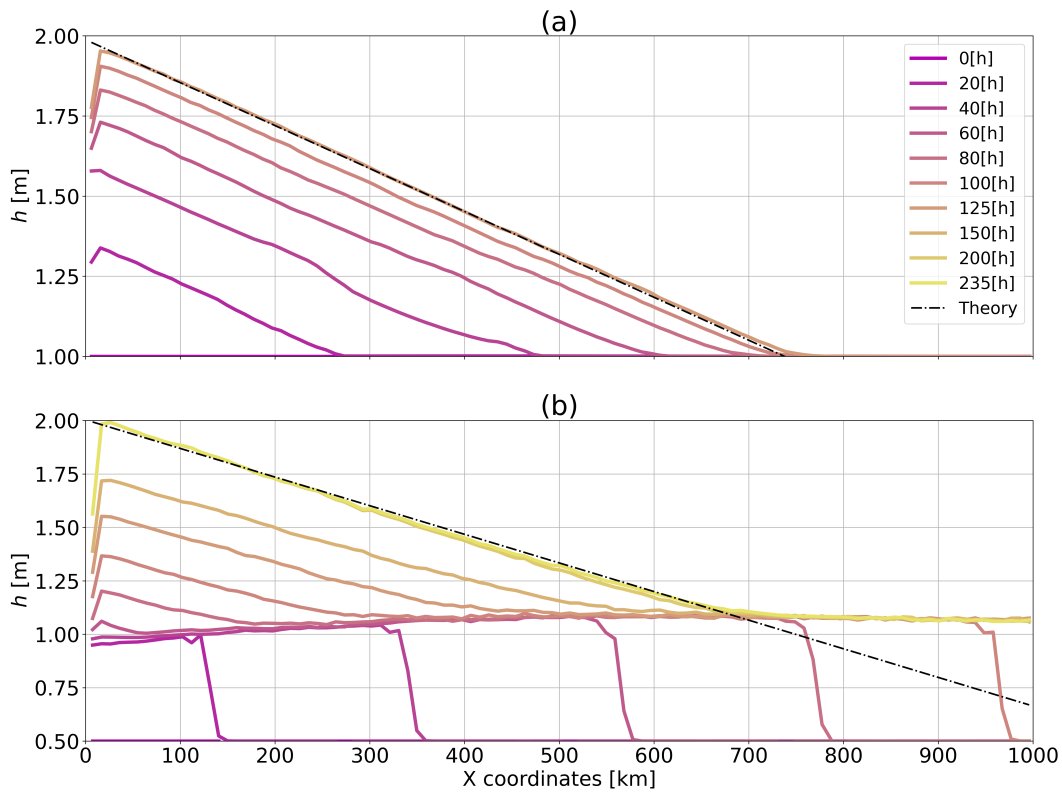
Figure 4.3: Temporal evolution of simulated sea-ice thickness along the central horizontal line of the domain for a) the ridge experiment initialized with a concentration $A = 1$ and average thickness $h = 1$ and b) the ridge experiment initialized with a concentration $A = 0.5$ and average thickness $h = 0.5$. The wall is located at $x = 0$ and the wind speed is $-5\hat{\mathbf{x}}\,[\mathrm{m}\cdot\mathrm{s}^{-1}]$. The theory follows Eq. (4.18).

ity equations in the context of SPH (Eqs. 3.28 - 3.29), we ensure that both h and A covary in time in such a way that $\frac{h}{A}$ remains constant in the MIZ until significant ice interactions take place. Results at $x = 300$ [km], away from the boundary effects, show that, as ex-

28

pected, thickness and concentration evolve coherently — h/A is constant in time or $\frac{\mathrm{d}(h/A)}{\mathrm{d}t}$ is zero — before ice concentration reaches $\approx 85\%$ (see Fig. 4.4 panel a). At that point ($t \approx 22$ [h]), the ice pack has sufficiently compacted to have an ice strength able to re-pulse the incoming particle and the ridging process starts ($\frac{\mathrm{d}(h/A)}{\mathrm{d}t} > 0$). The ridge build-up speed increase until a maximum concentration is reached after ≈ 70 [h] (see Fig. 4.4 panel c). Subsequently, the rate of advance of the ridge slows down with time as it takes more ice to be advected to build it up. When the ice thickness gradient is in balance with the surface wind stress (after ≈ 200 [h]), $\frac{\mathrm{d}(h/A)}{\mathrm{d}t}$ reaches steady state. Overall, we can observe 3 stages in the ridge formation (see Fig. 4.4). First, a rapid compaction stage, when ice particles are drifting close to their free drift speed since the ice strength is weak. Second, a transition stage between $A \approx 0.85 - 1$ when ridging occurs in the MIZ analogous to the wave radiation drag mentioned above. Third, a ridging stage with changes in ice thickness that are about one order of magnitude higher than the transition stage.

Note that oscillations (i.e., the ones between particles or coming from the boundaries) in both ridging experiments, diminish when incorporating the water drag. The force reduce efficiently the advection speed of the ice which results in less kinetic energy carried by the particles and fewer wobbles.
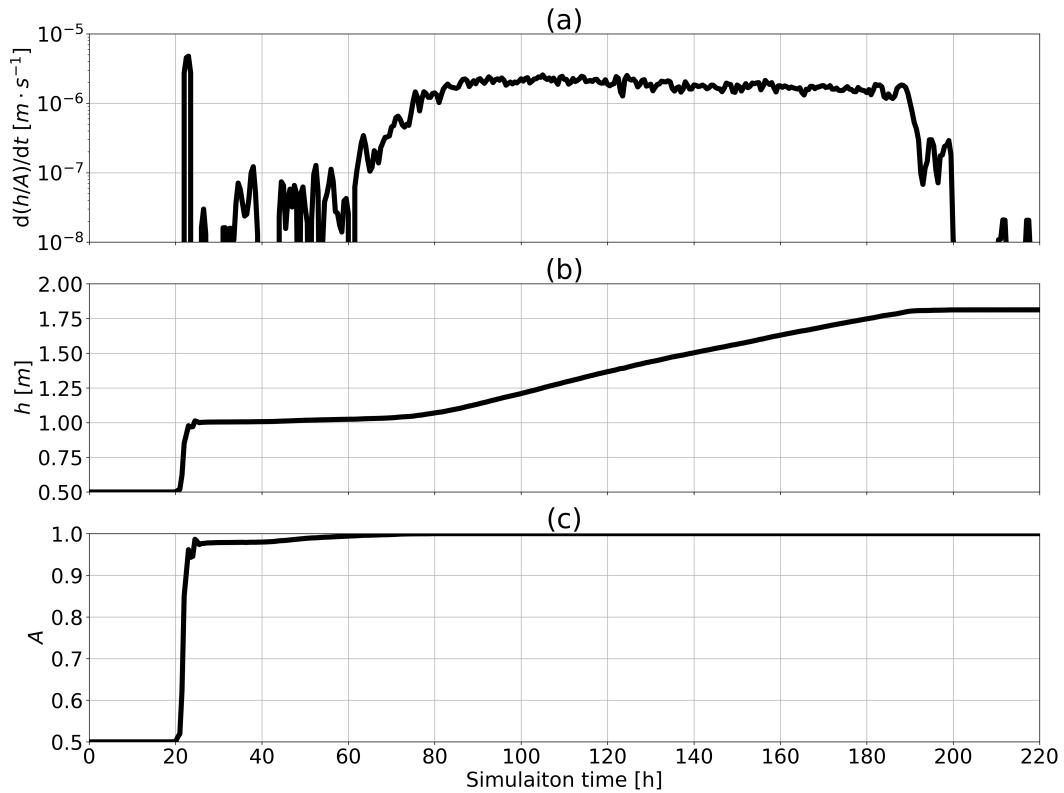
Figure 4.4: Evolution in time of a) the thickness normalized by concentration rate of change in time $\frac{d(h/A)}{dt}$, b) the average thickness h and c) the concentration A at $\mathbf{x} = 300$ [km]. The rate of change in time is computed from $\frac{df}{dt}(x,t) = \frac{f(x,t+\Delta t)-f(x,t-\Delta t)}{2\Delta t}$.

4.3 Arch experiments

We next compare the SPH approach with the FDM and DEM sea-ice model in a second well-studied idealized experiment: the ice arches formation. To this end, we run the SPH model in an idealized domain representing the Nares Strait (see Fig. 4.5) with an upstream reservoir 5 times the length of the channel (L) to minimize boundary confinement effect without sacrificing the spatial resolution.

The set of simulations uses a domain with $L = 60$ [km]. The initial condition for ice thickness, concentration and velocity are $h = 1$ [m], $A = 1$ and $\mathbf{u} = 0$ [m $\cdot$ s^{-1}]. The ice is forced with a constant unidirectional wind of -7.5 [m $\cdot$ s^{-1}] in the $\hat{\mathbf{y}}$-direction and ocean current is fixed to $\mathbf{u}_w = 0$ [m $\cdot$ s^{-1}]. The corresponding surface stress is ≈ 0.04 [kN $\cdot$ m^{-2}] and the total integrated stress at the entry of the channel is slightly smaller than P^* ($\int_0^{5L} \tau_a \mathrm{d}x =26.325$ [kN $\cdot$ m^{-1}]). We use a weaker wind than what is common in Nares Strait ice arches simulations (≈ 10 [m $\cdot$ s^{-1}]) to limit the ridging phase prior to the formation of the ice arch. In this experiment, we limit ourselves to ice with no tensile strength ($k_t = 0$) and a shear strength of 6.875 [kN $\cdot$ m^{-2}], i.e., an ellipse aspect ratio of 2. We first test whether the SPH approach has the same sensitivity to the relative size of particle with respect to the channel width as in DEM (Damsgaard et al., 2018). Results showed that no stable arch can be formed with the specified forcing for all particle diameter size tested (7.5, 5, 3.75 [km]) (see ice velocity field Fig.4.7). Instead, a "continuous" slow flow of ice is present in the channel. The discontinuity at the entry of the channel visible in the concentration, thickness and velocity fields (Fig. 4.7) can be interpreted as intermittent (unstable) ice arch formation. Also, we noted that larger particles are not more prone to ice jam than smaller ones. This is contrary to what is know from granular material theory and to results from Damsgaard et al. (2018) that show a transition from stable to no ice arch formation for floe sizes ranging from approximately one quarter to one sixteenth of the strait width. We explain this difference between SPH and DEM from
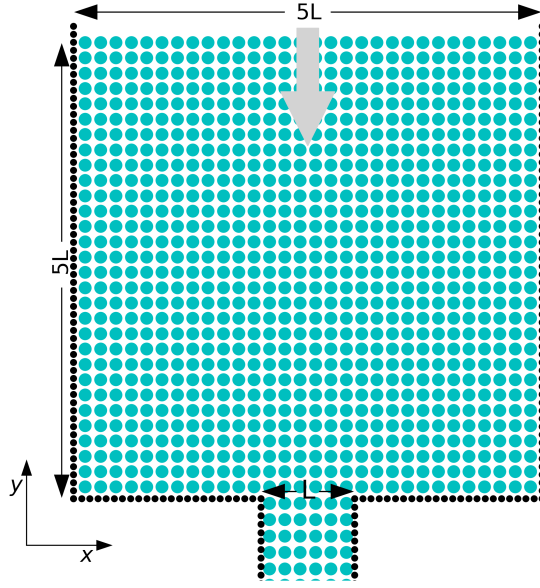
Figure 4.5: Idealized domain of the ice arch experiments. The blue circles represent the ice particles and the black ones are the boundary particles. The grey arrow shows the wind forcing.

the continuum description of the ice dynamics equation which describes the ice strength as a function of ice concentration and mean thickness, not on the particle size. Even though the increase in resolution — or particle size — has no effect on the arch stability, it enables smaller fractures resolution that are visible at the entrance of the channel (see ϵ_I and ϵ_{II} Fig. 4.6). In our SPH model, the stress invariants σ_I and σ_{II} shows oscillation patterns in regions where ice is in the viscous regime (see the tree-like structure in the normal and shear stress fields in Fig. 4.6). We hypothesized that those are associated with over-damped viscous waves occurring with small movement of the particle undergoing viscous deformation. Those structures are not symmetric, despite symmetrical initial conditions, because of the domino effect between interacting viscous waves. Note that they are absent from the strain-rate fields since viscous deformation are extremely small. They are also absent in sea-ice model based on a continuum approach (Dumont et al., 2009; Dansereau et al., 2017; Plante et al., 2020), but these tree-like structures are qualitatively

similar to the stress structure between floes observed in DEM (e.g., Damsgaard et al., 2018, Fig. 5c).
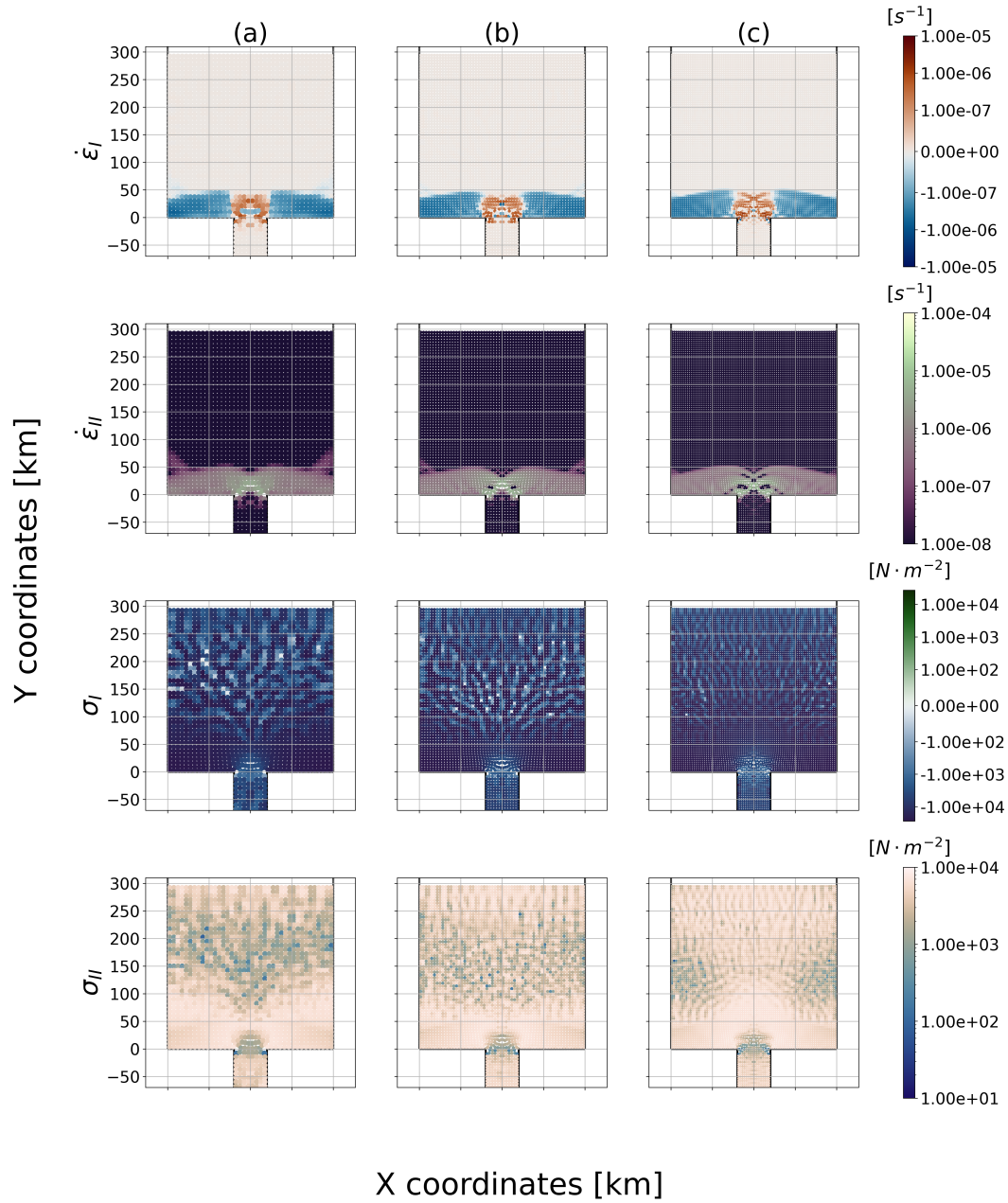

Figure 4.6: Strain rate and stress invariants ($\dot{\epsilon}_I$, $\dot{\epsilon}_{II}$, σ_I, σ_{II}) at time $t = 24$ [h] for an initial particle spacing of a) 7.5, b) 5 and c) 3.75 [km] (8, 12 and 16 particles can fit in the strait respectively) and the initial total integrated surface stress at the entry of the channel is 26.325 [kN $\cdot$ m^{-1}].
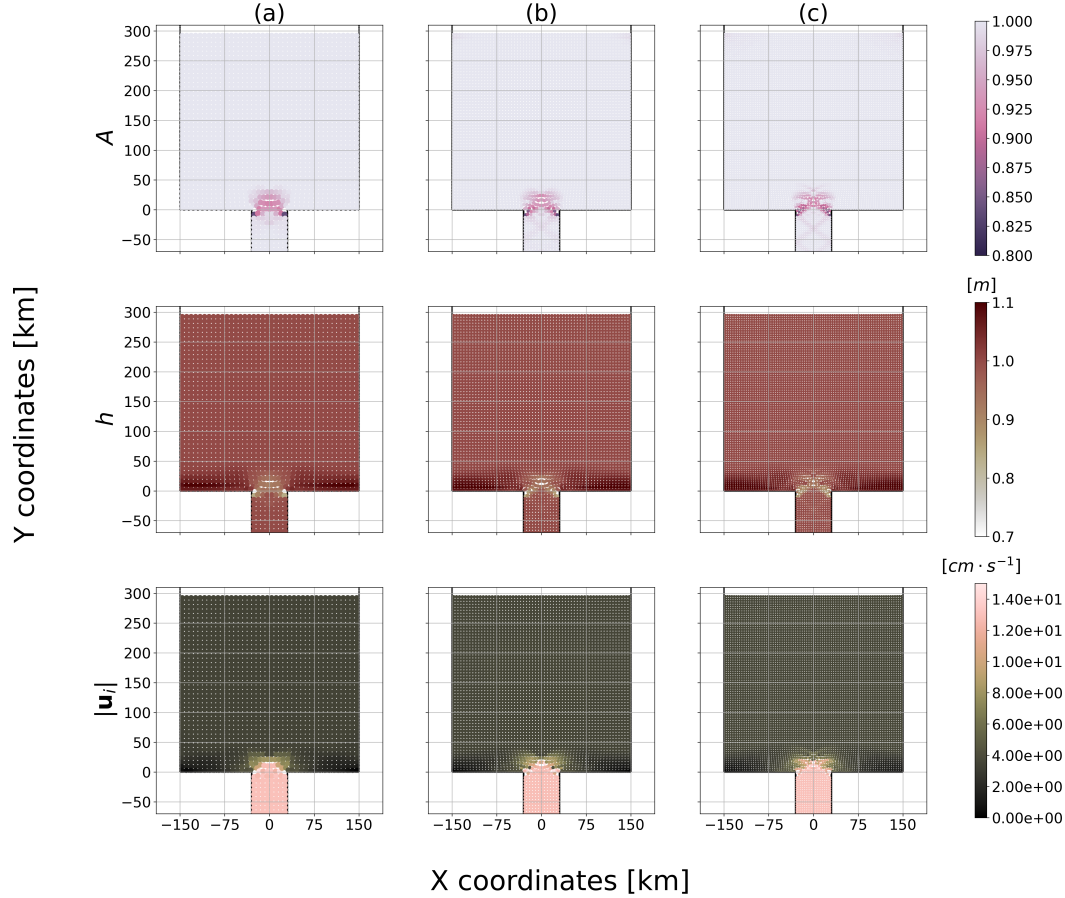
Figure 4.7: Ice concentration, thickness and total velocity (h, A, $|\mathbf{u}_i|$) at time $t = 24$ [h] for an initial particle spacing of a) 7.5, b) 5 and c) 3.75 [km] (8, 12 and 16 particles can fit in the strait respectively) and the initial total integrated surface stress at the entry of the channel is 26.325 [kN $\cdot$ m^{-1}].

Second, we explored the ability of the model to produce stable ice arches. To do so, we reduce the total integrated surface stress at the entry of the channel to 13.146 [kN $\cdot$ m^{-1}] (or 5.3 [m $\cdot$ s^{-1}]), which has the same effect as increasing the ice thickness. In this case, results show a clear stable arch (see Fig. 4.8) with a shape that is qualitatively similar to the one presented by Dansereau et al. (2017); Plante et al. (2020); West et al. (2022). It has been shown by Dumont et al. (2009) that the elliptical EVP rheology can only form stable arch for ellipse aspect ratio equal or lower than 1.8 ($e \leq 1.8$). Yet, in an SPH model, we are able to form one with $e = 2$. This suggests that SPH has a different sensitivity of ice arching to the ellipse aspect ratio e and ice thickness h. This behaviour may change

when using a no-slip boundary condition instead of free slip. Further investigation is left for future work. Nonetheless, this shows that SPH is able to capture large-scale features coming from small-scale interactions. The stable ice arch (Fig. 4.8) also shows how SPH can easily fracture and create discontinuity as seen in DEM models. Note that, in the SPH framework, a lead can be defined by particles far enough apart to not be in the support domain of each other — akin to DEM — or it can be defined by a set of particles with neighbours, but with a concentration and an average thickness of 0 — akin to FDM. To make an analogy of the lead formation in SPH with the continuum framework, it is as if a grid splits up at the location of the fracture creating new edges in the domain. This is a similar behaviour as the elastic-decohesive sea-ice constitutive model explored by Schreyer et al. (2006) or the FEM model of Rampal et al. (2016).
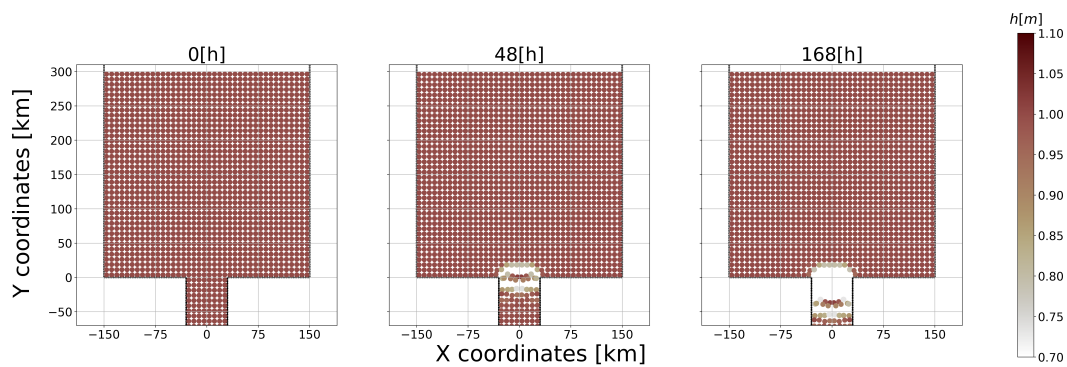

Figure 4.8: Thickness field at time $t = 0, 48, 168$ [h] for an initial particle spacing of 7.5 [km] and a total integrated stress at the entry of the channel of 13.146 [kN $\cdot$ m^{-1}].

Chapter 5

Conclusions and Summary

In this paper, we have presented a first implementation of the Viscous-Plastic rheology with an elliptical yield curve and normal flow rule in the framework of SPH with the long-term goal of simulating synoptic scale sea-ice dynamics. We have described the basics of the SPH approach and how the sea-ice dynamic equations can be formulated in this framework along with the implementation of key components of the numerical method such as the smoothing length, the kernel, the boundaries and the time integration technique. We proposed a different definition of the particle density and showed that the more commonly used density definition involving the ice concentration when used together with the average ice thickness leads to erroneous plastic wave speed propagation. A particle density definition independent of the ice concentration corrects this and leads to results that are inline with the VP theory. The SPH model thus developed is in excellent agreement (error of $\approx 1\%$) with an analytical solution of the VP ice dynamic for a simple 1D ridging experiment. The approximations used at the core of the SPH framework, result in a dispersive plastic wave speed in the medium — contrary to its FDM counterpart — which is dependent on the smoothing length (or resolution) and the choice of the kernel. The plastic wave speed is mostly affected for wavelengths 11 times the smoothing length and lower.

From the simple ridging experiment with fixed sea-ice concentration ($A = 1$), we observe nonphysical damped oscillations that propagate in the domain associated with our choice of boundary conditions. The conclusions drawn from our simulations are robust to the choice of boundary conditions. Nevertheless, this behaviour needs to be removed for a proper simulation of sea-ice near coastlines. The ridging experiment with an initial ice concentration below 100% showed that continuity equations for concentration and thickness evolve coherently until a concentration of 85%. At that point, SPH particles start to ridge locally in the MIZ in addition to the wall where the maximum stress is located. This effect is not observed in continuum approach and is presumably related to particle collisions in converging motion.

When compared to other numerical framework, the SPH model is able to reproduce stable ice arches in an idealized domain of a strait with an ellipse aspect ratio of 2 and a wind forcing of 5.3 $[\mathrm{m \cdot s^{-1}}]$, contrary to other continuum approaches that require higher material shear strength. However, when using a stronger wind field of 7.5 $[\mathrm{m \cdot s^{-1}}]$, no stable arches are formed when increasing the particles size in the strait (stable arches are only achieved when increasing particle average thickness). We concluded that the number of particles in the strait does not influence the formation of ice arches contrary to DEM and is analogous to an increase in resolution in a continuum framework : a larger number of particles influence the number of fractures that can form and the resolution of fine-scale structures. The stress fields produced by the SPH model in the channel experiment show tree-like pattern upstream of the channel where there are low total deformations. This is not observed in FDM experiment but is qualitatively similar to tensile stress network exhibited in DEM (Damsgaard et al., 2018) that comes from individual contact force between the ice floes and is hypothesized to be associated with damped viscous sound waves.

Even though we successfully implemented the standard sea-ice Viscous-Plastic rheology with an elliptical yield curve and a normal flow rule in an SPH framework, the current

model does not outperform classical FDM model. In fact, there are inherent difficulties and instabilities in SPH that do not exist in FDM. It is known that the SPH framework trade consistency — i.e., the ability to correctly represent a differential equation in the limit of an infinite number of points with a null spacing between them — for stability , which gives the SPH a distinct feature of working well for many complicated problems with good efficiency, but less accuracy. However, the classical formulation of SPH used and described in the present work does not usually respect zeroth-order consistency because of the unstructured particle position in space(see Belytschko et al., 1998, section 3 for derivation). Nevertheless, consistency can be improved at the expense of computational cost (Chen, Beraun, 2000; Liu et al., 2003) by reformulating the SPH core approximation (Eq. 3.1). Also, boundary description has been identified as a weak point of the SPH framework since prescribing a Dirichlet or Neumann boundary condition is not as straightforward as in continuum approaches and preventing particle penetration through a boundary is still a challenging task (Liu, Liu, 2010) and the SPH consistency is usually at its worst at the boundary because the support domain is truncated. In the present study, a proper physical representation of the boundary was not adopted and the boundary treatment was chosen for its numerical simplicity and should be modified in future work. Other major issues with SPH are the zero-energy modes and the tensile instability previously mentioned. The zero-energy modes can be found in FDM and FEM and they correspond to modes at which the strain energy calculated is erroneously zero (Swegle et al., 1995). The tensile instability results in particle clumping or nonphysical fractures in the material. In the present work, we adopted a different kernel from the usual Gaussian spline to avoid those instabilities, but other methods such as the independent stress point (Dyka, Ingel, 1995; Chalk et al., 2020), artificial short length repulsive force (Monaghan, 2000), particle repositioning (Sun et al., 2018), adaptive kernel (Lahiri et al., 2020), etc. can be used if more stabilization is needed. For example, at smaller scale, SPH simulation of ice in uniaxial compression was improved by a simplified finite difference interpolation scheme (Zhang et al., 2017). More specifically for sea-ice model, Kreyscher et al.

(2000) pressure closure is not well suited for long simulation. Indeed, particle can still move when they are in the viscous state but, have low internal ice pressure because of the replacement pressure scheme. Consequently, particles could pass through each other resulting in erroneous location of the parameters carried. Finally, using SPH for sea-ice modules in grid-based continuum global climate model (GCM) complicates the coupling with ocean and atmosphere components since particle quantities need to be converted on a grid and vice versa.

Nevertheless, SPH also has interesting properties that could be exploited. For example, SPH can be used with little change for problems involving several fluids whether liquid, gas, or dust fluids (Monaghan, 2012). This feature could be exploited in the creation of a general approach for all components of a GCM (atmosphere, ocean and sea-ice). The method developed is also a proper option for nowcasting sea-ice prediction because only the ice dynamics need to be considered in nowcasting applications and the model has a good ability to carry the ice property in space. SPH can fracture and transitions from the continuum to fragments seamlessly, which is the main reason for our investigation of the method for sea-ice dynamics. The elastic behaviour assumed for sea-ice in certain rheology can be associated to the weak compressibility inherent in the classical formulation of SPH. Finally, the SPH discretization of the continuum into particles enables the implementation of several new features. For example, angular momentum to individual floes (or pack of floes) can be added to take into account rotation along LKFs. A direct measure of the concentration from the number of particles within a support domain (this takes advantages of already computed number of neighbours and help ensuring the desired number of neighbours in converging flow) can be computed. A subscale parametrization of floe-floe contact force (this short length repulsive force could also help for the tensile instability) can be implemented. A varying floe size distribution can be incorporated by varying the mass carried by a particle for a given particle density.

For future work, a more physical boundary treatment should be investigated — e.g., using the immerse boundary method (Tu et al., 2018) with a fixed grid for the boundary and an interpolation scheme to apply force on the particle to simulate the grounding of sea-ice near the coast. Additionally, to generalize the model for pan-arctic simulation, the Coriolis and sea surface tilt force along with the treatment of the thermodynamics sources and sinks needs to be implemented in the framework (work already started by Staroszczyk, 2018). The computation speed should be made comparable to the FDM models and, to do so, improving the algorithm parallelization is required. The current work began the study of perturbations coming from the SPH framework in the context of sea-ice, nonetheless a deeper inspection of the stability and accuracy of the method should be done. All in all, there is a lot of work remaining for the development of an SPH sea-ice model able to compete with current state-of-the-art continuum sea-ice models, but the method has shown to be a promising tool to investigate sea-ice material properties.

Chapter 6

Appendix

6.1 Derivations of vector operator in SPH

Vector operator takes different forms in the SPH framework because they only operate on the smoothing kernel W. Also, to make sure the interaction between particles is symmetric, the operator form is changed so both particles (the current one and its interacting neighbours) interact in the same way. The following subsection shows the demonstrations.

6.1.1 Divergence of a vector

First to symmetries this operator we rewrite the divergence of vector as follows using the identity of the divergence of a scalar function times a vector and chose the scalar function to be density:

$$\nabla \cdot \vec{V} = \frac{1}{\rho}\left(\nabla \cdot (\rho \vec{V}) - \vec{V} \cdot \nabla \rho\right). \tag{6.1}$$

Now forgetting about equation (6.1) and applying the integral interpolant approximation (3.1) to the divergence of density times a vector and to the density gives us the two

following equation:

$$\nabla \cdot (\rho \vec{V}) = \int_{\mathcal{V}} \nabla' \cdot (\rho' \vec{V}') W \ d\vec{r'} = \int_{\mathcal{V}} \nabla' \cdot (\rho' \vec{V}' W) d\vec{r'} - \int_{\mathcal{V}} \rho' \vec{V}' \cdot \nabla' W \, d\vec{r'}, \tag{6.2}$$

$$\rho = \int_{\mathcal{V}} \rho' W \, d\vec{r'}. \tag{6.3}$$

In the above equation, the prime quantities are used to show that they are functions of the whole space, in contrast to the quantities with no primes which refer to a specific location in space. The kernel is the only function that depends on both primed and non-primed position as defined at (3.1). Using divergence theorem it is possible to cancel the first term in (6.2) by the following :

$$\int_{\mathcal{V}} \nabla' \cdot (\rho' \vec{V}' W) d\vec{r'} = \int_{\mathcal{S}} (\rho' \vec{V}' W) \cdot d\vec{s'} = 0. \tag{6.4}$$

In the equation (6.4), $\vec{s'}$ denotes an infinitesimal area element and $\mathcal{S}$ is the surface encompassing the volume $\mathcal{V}$. The term is null because of the compact support of the kernel ($W = 0$ at the edge of the domain). Now using the particle approximation (3.4) the equations (6.2) and (6.3) are written as:

$$(\nabla \cdot (\rho \vec{V}))_p = - \sum_q m_q \vec{V}_q \cdot \nabla_q W_{pq} = \sum_q m_q \vec{V}_q \cdot \nabla_p W_{pq}, \tag{6.5}$$

$$\rho_p = \sum_q m_q W_{pq}, \tag{6.6}$$

where we used the identity $\nabla_p = -\nabla_q$ and p and q represent the current particle referential and the neighbour one respectively. Finally, substituting the last two equations (6.5, 6.6) in the first one that we let behind (6.1) gives the desired form :

$$(\nabla \cdot \vec{V})_p = \frac{1}{\rho_p} \left(\sum_q m_q \vec{V}_q \cdot \nabla_p W_{pq} - \vec{V}_p \cdot \nabla_p \sum_q m_q W_{pq} \right) \tag{6.7}$$

$$= \frac{1}{\rho_p} \left(\sum_q m_q (\vec{V}_q - \vec{V}_p) \cdot \nabla W_{pq}. \right) \tag{6.8}$$

6.1.2 Divergence of a 2D tensor field

In the following demonstration, we used the Einstein summation convention to simplify the calculation and the tensor representation. So, let's start by writing the divergence of a 2D tensor divided by the density to have the following equation:

$$\frac{\partial}{\partial x_i}\left(\frac{T_{ij}}{\rho}\right) = \frac{1}{\rho}\frac{\partial T_{ij}}{\partial x_i} - \frac{T_{ij}}{\rho^2}\frac{\partial \rho}{\partial x_i}. \tag{6.9}$$

Reorganizing the terms gives :

$$\frac{\partial T_{ij}}{\partial x_i} = \rho\left[\frac{\partial}{\partial x_i}\left(\frac{T_{ij}}{\rho}\right) + \frac{T_{ij}}{\rho^2}\frac{\partial \rho}{\partial x_i}\right]. \tag{6.10}$$

Now applying the interpolant approximation (3.1) to the first term in the bracket leads to :

$$\frac{\partial}{\partial x_i}\left(\frac{T_{ij}}{\rho}\right) = \int_{\mathcal{V}} \frac{\partial}{\partial x_i'}\left(\frac{T_{ij}'}{\rho'}\right) W \ d\vec{r'} \tag{6.11}$$

$$= \int_{\mathcal{V}} \frac{\partial}{\partial x_i'}\left(\frac{T_{ij}'}{\rho'}W\right) d\vec{r'} - \int_{\mathcal{V}} \left(\frac{T_{ij}'}{\rho'}\right)\frac{\partial W}{\partial x_i'}d\vec{r'}. \tag{6.12}$$

As for the divergence of a vector demonstration (section 6.1.1), the first integral above vanish by using the divergence theorem since the kernel has a compact support domain. Therefore, applying the particle approximation to the above equation leads to :

$$\left(\frac{\partial}{\partial x_i}\left(\frac{T_{ij}}{\rho}\right)\right)_p = -\sum_q \left(m_q\frac{(T_{ij})_q}{\rho_q^2}\right)\frac{\partial W_{pq}}{\partial (x_i)_q} = \sum_q \left(m_q\frac{(T_{ij})_q}{\rho_q^2}\right)\frac{\partial W_{pq}}{\partial (x_i)_p}. \tag{6.13}$$

Substituting this in the equation 6.9 and using the equality 6.6 for the density in the gradient operator, in the last term, we get the following expression :

$$\left(\frac{\partial T_{ij}}{\partial x_i}\right)_p = \rho_p \left[\sum_q \left(m_q \frac{(T_{ij})_q}{\rho_q^2}\right)\frac{\partial W_{pq}}{\partial(x_i)_p} + \frac{(T_{ij})_p}{\rho_p^2}\frac{\partial}{\partial(x_i)_p}\left(\sum_q m_q W_{pq}\right)\right] \tag{6.14}$$

$$= \rho_p \left[\sum_q m_q \left(\frac{(T_{ij})_q}{\rho_q^2} + \frac{(T_{ij})_p}{\rho_p^2}\right)\frac{\partial W_{pq}}{\partial(x_i)_p}\right] \tag{6.15}$$

$$= \rho_p \sum_q m_q \left(\frac{\vec{T_q}}{\rho_q^2} + \frac{\vec{T_p}}{\rho_p^2}\right)\cdot\nabla_p W_{pq}, \tag{6.16}$$

which is the form presented at equation (3.6).

6.1.3 Gradient of a vector field

To demonstrate the equation (3.7) we first have to recall that the zeroth-order moment of the kernel equals 1 and it can be written as :

$$M_0 = \int_{\mathcal{V}} W(\vec{r} - \vec{r'}, l_p)d\vec{r'} = 1 \tag{6.17}$$

$$= \sum_q \frac{m_q}{\rho_q} W_{pq}, \tag{6.18}$$

where the particle approximation (3.4) was used to rewrite the integral. Using this identity it is possible to write:

$$\nabla(\vec{V}1) = 1\nabla\vec{V} + \vec{V}\cdot\nabla 1 \tag{6.19}$$

$$= \nabla\vec{V} - \vec{V}\cdot\nabla 1. \tag{6.20}$$

Now, using the particle approximation (3.4) on $\vec{V}$ and substituting the 1 with the zeroth moment identity in the expression 6.20 we get:

$$(\nabla \vec{V})_p = \frac{\partial}{\partial (x_i)_p} \sum_q \frac{m_q}{\rho_q} (V_j)_q W_{pq} - (V_j)_p \frac{\partial}{\partial (x_i)_p} \sum_q \frac{m_q}{\rho_q} W_{pq} \tag{6.21}$$

$$= \sum_q \frac{m_q}{\rho_q} ((V_j)_q - (V_j)_p) \frac{\partial}{\partial (x_i)_p} W_{pq} \tag{6.22}$$

$$= \sum_q \frac{m_q}{\rho_q} (\vec{V_q} - \vec{V_p}) \otimes \nabla_p W_{pq}, \tag{6.23}$$

where Einstein summation convention was once again used to simplify the derivation.

Bibliography

Aagaard Knut, Coachman L.K., Carmack Eddy. On the halocline of the Arctic Ocean // Deep Sea Research Part A. Oceanographic Research Papers. VI 1981. 28, 6. 529–545.

Adcroft Alistair, Anderson Whit, Balaji V., Blanton Chris, Bushuk Mitchell, Dufour Carolina O., Dunne John P., Griffies Stephen M., Hallberg Robert, Harrison Matthew J., Held Isaac M., Jansen Malte F., John Jasmin G., Krasting John P., Langenhorst Amy R., Legg Sonya, Liang Zhi, McHugh Colleen, Radhakrishnan Aparna, Reichl Brandon G., Rosati Tony, Samuels Bonita L., Shao Andrew, Stouffer Ronald, Winton Michael, Wittenberg Andrew T., Xiang Baoqiang, Zadeh Niki, Zhang Rong. The GFDL Global Ocean and Sea Ice Model OM4.0: Model Description and Simulation Features // Journal of Advances in Modeling Earth Systems. X 2019. 11, 10. 3167–3211.

Arrigo Kevin R. Annual cycles of sea ice and phytoplankton in Cape Bathurst polynya, southeastern Beaufort Sea, Canadian Arctic // Geophysical Research Letters. 2004. 31, 8.

Beatty Christof König, Holland David M. Modeling landfast sea ice by adding tensile strength // Journal of Physical Oceanography. I 2010. 40, 1. 185–198. Copyright: Copyright 2010 Elsevier B.V., All rights reserved.

Belytschko T., Krongauz Y., Dolbow J., Gerlach C. On the completeness of meshfree particle methods // International Journal for Numerical Methods in Engineering. XI 1998. 43, 5. 785–819.

Bouchat Amélie, Hutter Nils, Chanut Jérôme, Dupont Frédéric, Dukhovskoy Dmitry, Garric Gilles, Lee Younjoo J., Lemieux Jean-François, Lique Camille, Losch Martin, Maslowski Wieslaw, Myers Paul G., Ólason Einar, Rampal Pierre, Rasmussen Till, Talandier Claude, Tremblay Bruno, Wang Qiang. Sea Ice Rheology Experiment (SIREx): 1. Scaling and Statistical Properties of Sea-Ice Deformation Fields // Journal of Geophysical Research: Oceans. IV 2022. 127, 4.

Bouchat Amélie, Tremblay Bruno. Using sea-ice deformation fields to constrain the mechanical strength parameters of geophysical sea ice // Journal of Geophysical Research: Oceans. VII 2017. 122, 7. 5802–5825.

Budikova Dagmar. Role of Arctic sea ice in global atmospheric circulation: A review // Global and Planetary Change. VIII 2009. 68, 3. 149–163.

Cavelan Aurélien, Cabezón Rubén M., Korndorfer Jonas H. M., Ciorba Florina M. Finding Neighbors in a Forest: A b-tree for Smoothed Particle Hydrodynamics Simulations. 2019.

Chalk C.M., Pastor M., Peakall J., Borman D.J., Sleigh P.A., Murphy W., Fuentes R. Stress-Particle Smoothed Particle Hydrodynamics: An application to the failure and post-failure behaviour of slopes // Computer Methods in Applied Mechanics and Engineering. VII 2020. 366. 113034.

Chen J.K., Beraun J.E. A generalized smoothed particle hydrodynamics method for nonlinear dynamic problems // Computer Methods in Applied Mechanics and Engineering. X 2000. 190, 1-2. 225–239.

Coon Max, Kwok Ron, Levy Gad, Pruis Matthew, Schreyer Howard, Sulsky Deborah. Arctic Ice Dynamics Joint Experiment (AIDJEX) assumptions revisited and found inadequate // Journal of Geophysical Research. XI 2007. 112, C11.

Damsgaard A., Adcroft A., Sergienko O. Application of Discrete Element Methods to Approximate Sea Ice Dynamics // Journal of Advances in Modeling Earth Systems. IX 2018. 10, 9. 2228–2244.

Dansereau Véronique, Weiss Jérôme, Saramito Pierre, Lattes Philippe. A Maxwell elasto-brittle rheology for sea ice modelling // The Cryosphere. VII 2016. 10, 3. 1339–1359.

Dansereau Véronique, Weiss Jérôme, Saramito Pierre, Lattes Philippe, Coche Edmond. Ice bridges and ridges in the Maxwell-EB sea ice rheology // The Cryosphere. IX 2017. 11, 5. 2033–2058.

Dehnen Walter, Aly Hossam. Improving convergence in smoothed particle hydrodynamics simulations without pairing instability // Monthly Notices of the Royal Astronomical Society. 09 2012. 425, 2. 1068–1082.

Dethleff Dirk. Polynyas as a Possible Source for Enigmatic Bennett Island Atmospheric Plumes // The Polar Oceans and Their Role in Shaping the Global Environment. III 2013. 475–483.

Dumont Dany, Gratton Yves, Arbetter Todd E. Modeling the Dynamics of the North Water Polynya Ice Bridge // Journal of Physical Oceanography. VI 2009. 39, 6. 1448–1461.

Dyka C.T., Ingel R.P. An approach for tension instability in smoothed particle hydrodynamics (SPH) // Computers &amp Structures. XI 1995. 57, 4. 573–580.

Fichefet T., Maqueda M. A. Morales. Sensitivity of a global sea ice model to the treatment of ice thermodynamics and dynamics // Journal of Geophysical Research: Oceans. VI 1997. 102, C6. 12609–12646.

Fleissner Florian, Gaugele Timo, Eberhard Peter. Applications of the discrete element method in mechanical engineering // Multibody System Dynamics. VI 2007. 18, 1.

Fraga Filho Carlos Alberto. Smoothed Particle Hydrodynamics: Fundamentals and Basic Applications in Continuum Mechanics. 01 2019.

Gardner Alex S., Sharp Martin J. A review of snow and ice albedo and the development of a new physically based broadband albedo parameterization // Journal of Geophysical Research. III 2010. 115, F1.

Gingold R. A., Monaghan J. J. Smoothed particle hydrodynamics: theory and application to non-spherical stars // Monthly Notices of the Royal Astronomical Society. XII 1977. 181, 3. 375–389.

Girard Lucas, Bouillon Sylvain, Weiss Jérôme, Amitrano David, Fichefet Thierry, Legat Vincent. A new modeling framework for sea-ice mechanics based on elasto-brittle rheology // Annals of Glaciology. 2011. 52, 57. 123–132.

Gray J., Morland L.W. A Two-Dimensional Model for the Dynamics of Sea Ice // Philosophical Transactions of The Royal Society B: Biological Sciences. 04 1994. 347. 219–290.

Gray J. M. N. T. Loss of Hyperbolicity and Ill-posedness of the Viscous–Plastic Sea Ice Rheology in Uniaxial Divergent Flow // Journal of Physical Oceanography. XI 1999. 29, 11. 2920–2929.

Gutfraind Ricardo, Savage Stuart B. Smoothed Particle Hydrodynamics for the Simulation of Broken-Ice Fields: Mohr–Coulomb-Type Rheology and Frictional Boundary Conditions // Journal of Computational Physics. VII 1997. 134, 2. 203–215.

Haid V., Timmermann R. Simulated heat flux and sea ice production at coastal polynyas in the southwestern Weddell Sea // Journal of Geophysical Research: Oceans. V 2013. 118, 5. 2640–2652.

Herman Agnieszka. Discrete-Element bonded-particle Sea Ice model DESIgn, version 1.3a – model description and implementation // Geoscientific Model Development. IV 2016. 9, 3. 1219–1241.

Hibler W. D. A Dynamic Thermodynamic Sea Ice Model // Journal of Physical Oceanography. VII 1979. 9, 4. 815–846.

Hopkins Mark A., Thorndike Alan S. Floe formation in Arctic sea ice // Journal of Geophysical Research. 2006. 111, C11.

Hosseini Khosrow, Omidvar Pourya, Kheirkhahan Mehran, Farzin Saeed. Smoothed particle hydrodynamics for the interaction of Newtonian and non-Newtonian fluids using the (I) model // Powder Technology. VI 2019. 351. 325–337.

Hunke E. C., Dukowicz J. K. An Elastic–Viscous–Plastic Model for Sea Ice Dynamics // Journal of Physical Oceanography. IX 1997. 27, 9. 1849–1867.

Hutter Nils, Bouchat Amélie, Dupont Frédéric, Dukhovskoy Dmitry, Koldunov Nikolay, Lee Younjoo J., Lemieux Jean-François, Lique Camille, Losch Martin, Maslowski Wieslaw, Myers Paul G., Ólason Einar, Rampal Pierre, Rasmussen Till, Talandier Claude, Tremblay Bruno, Wang Qiang. Sea Ice Rheology Experiment (SIREx): 2. Evaluating Linear Kinematic Features in High-Resolution Sea Ice Simulations // Journal of Geophysical Research: Oceans. IV 2022. 127, 4.

Ji Shunying, Shen Hung, Wang Z., Shen Hayley, Yue Q. A viscoelastic-plastic constitutive model with Mohr-Coulomb yielding criterion for sea ice dynamics // Acta Oceanologica Sinica. 01 2005. 24. 54–65.

Johnson G. R., Beissel S. R. NORMALIZED SMOOTHING FUNCTIONS FOR SPH IMPACT COMPUTATIONS // International Journal for Numerical Methods in Engineering. 1996. 39, 16. 2725–2741.

Kalenitchenko Dimitri, Joli Nathalie, Potvin Marianne, Tremblay Jean-Éric, Lovejoy Connie. Biodiversity and Species Change in the Arctic Ocean: A View Through the Lens of Nares Strait // Frontiers in Marine Science. VIII 2019. 6.

Kottmeier Ch., Engelbart D. Generation and atmospheric heat exchange of coastal polynyas in the Weddell Sea // Boundary-Layer Meteorology. VIII 1992. 60, 3. 207–234.

Kreyscher Martin, Harder Markus, Lemke Peter, Flato Gregory M. Results of the Sea Ice Model Intercomparison Project: Evaluation of sea ice rheology schemes for use in climate simulations // Journal of Geophysical Research: Oceans. V 2000. 105, C5. 11299–11320.

Lahiri Saptarshi Kumar, Bhattacharya Kanishka, Shaw Amit, Ramachandra L S. A stable SPH with adaptive B-spline kernel // ArXiv. 2020. abs/2001.03416.

Lemieux Jean-François, Tremblay Bruno. Numerical convergence of viscous-plastic sea ice models // Journal of Geophysical Research. V 2009. 114, C5.

Lilja Ville-Pekka, Polojärvi Arttu, Tuhkuri Jukka, Paavilainen Jani. Finite-discrete element modelling of sea ice sheet fracture // International Journal of Solids and Structures. V 2021. 217-218. 228–258.

Lipscomb William H., Hunke Elizabeth C., Maslowski Wieslaw, Jakacki Jaromir. Ridging, strength, and stability in high-resolution sea ice models // Journal of Geophysical Research. III 2007. 112, C3.

Liu G.R., Liu M.B. Smoothed Particle Hydrodynamics: A Meshfree Particle Method. 2003.

Liu M. B., Liu G. R. Smoothed Particle Hydrodynamics (SPH): an Overview and Recent Developments // Archives of Computational Methods in Engineering. II 2010. 17, 1. 25–76.

Liu M. B., Liu G. R., Lam K. Y. A one-dimensional meshfree particle formulation for simulating shock waves // Shock Waves. XI 2003. 13, 3. 201–211.

Losch Martin, Menemenlis Dimitris, Campin Jean-Michel, Heimbach Patick, Hill Chris. On the formulation of sea-ice models. Part 1: Effects of different solver implementations and parameterizations // Ocean Modelling. I 2010. 33, 1-2. 129–144.

Lucy L. B. A numerical approach to the testing of the fission hypothesis // The Astronomical Journal. XII 1977. 82. 1013.

Maqueda M. A. Morales. Polynya Dynamics: a Review of Observations and Modeling // Reviews of Geophysics. 2004. 42, 1.

Maykut Gary A. Large-scale heat exchange and ice production in the central Arctic // Journal of Geophysical Research. 1982. 87, C10. 7971.

McPhee Miles G. The Effect of the Oceanic Boundary Layer on the Mean Drift of Pack Ice: Application of a Simple Model // Journal of Physical Oceanography. III 1979. 9, 2. 388–400.

Mehlmann C., Danilov S., Losch M., Lemieux J. F., Hutter N., Richter T., Blain P., Hunke E. C., Korn P. Simulating Linear Kinematic Features in Viscous-Plastic Sea Ice Models on Quadrilateral and Triangular Grids With Different Variable Staggering // Journal of Advances in Modeling Earth Systems. X 2021. 13, 11.

Monaghan J J. Smoothed particle hydrodynamics // Reports on Progress in Physics. VII 2005. 68, 8. 1703–1759.

Monaghan J.J. SPH without a Tensile Instability // Journal of Computational Physics. IV 2000. 159, 2. 290–311.

Monaghan J.J. Smoothed Particle Hydrodynamics and Its Diverse Applications // Annual Review of Fluid Mechanics. 2012. 44, 1. 323–346.

Monaghan J.J., Kajtar J.B. SPH particle boundary forces for arbitrary boundaries // Computer Physics Communications. 2009. 180, 10. 1811–1820.

Morland L. W., Staroszczyk R. A material coordinate treatment of the sea–ice dynamics equations // Proceedings of the Royal Society of London. Series A: Mathematical, Physical and Engineering Sciences. XI 1998. 454, 1979. 2819–2857.

Morris Joseph P., Fox Patrick J., Zhu Yi. Modeling Low Reynolds Number Incompressible Flows Using SPH // Journal of Computational Physics. 1997. 136, 1. 214–226.

Natanson I. P. Theory of Functions of a Real Variable. 2. New York: Frederick Ungar Publishing Co., 1961. 11 – 21.

Ohshima Kay I., Nihashi Sohey, Iwamoto Katsushi. Global view of sea-ice production in polynyas and its linkage to dense/bottom water formation // Geoscience Letters. V 2016. 3, 1.

Overland James E., McNutt S. Lyn, Salo Sigrid, Groves Joanne, Li Shusun. Arctic sea ice as a granular plastic // Journal of Geophysical Research: Oceans. IX 1998. 103, C10. 21845–21867.

Peiró Joaquim, Sherwin Spencer. Finite difference, finite element and finite volume methods for partial differential equations // Handbook of materials modeling. 2005. 2415–2446.

Plante Mathieu, Tremblay Bruno, Losch Martin, Lemieux Jean-François. Landfast sea ice material properties derived from ice bridge simulations using the Maxwell elasto-brittle rheology // The Cryosphere. VII 2020. 14, 6. 2137–2157.

Rabatel Matthias, Labbé Stéphane, Weiss Jérôme. Dynamics of an assembly of rigid ice floes // Journal of Geophysical Research: Oceans. IX 2015. 120, 9. 5887–5909.

Rampal Pierre, Bouillon Sylvain, Ólason Einar, Morlighem Mathieu. neXtSIM: a new Lagrangian sea ice model // The Cryosphere. V 2016. 10, 3. 1055–1073.

Ranta Janne, Polojärvi Arttu, Tuhkuri Jukka. Limit mechanisms for ice loads on inclined structures: Buckling // Cold Regions Science and Technology. III 2018. 147. 34–44.

Rhoades Clifford E. A fast algorithm for calculating particle interactions in smooth particle hydrodynamic simulations // Computer Physics Communications. VII 1992. 70, 3. 478–482.

Ringeisen Damien, Losch Martin, Tremblay L. Bruno, Hutter Nils. Simulating intersection angles between conjugate faults in sea ice with different viscous–plastic rheologies // The Cryosphere. IV 2019. 13, 4. 1167–1186.

Salehizadeh A. M., Shafiei A. R. Modeling of granular column collapses with (I) rheology using smoothed particle hydrodynamic method // Granular Matter. III 2019. 21, 2.

Schreyer H. L., Sulsky D. L., Munday L. B., Coon M. D., Kwok R. Elastic-decohesive constitutive model for sea ice // Journal of Geophysical Research. X 2006. 111, C11.

Schulson Erland M. Compressive shear faults within arctic sea ice: Fracture on scales large and small // Journal of Geophysical Research. 2004. 109, C7.

Sheikh Bahman, Qiu Tong, Ahmadipur Amir. Comparison of SPH boundary approaches in simulating frictional soil–structure interaction // Acta Geotechnica. X 2020. 16, 8. 2389–2408.

Shen Hung Tao, Shen Hayley, Tsai Shi-Ming. Dynamic transport of river ice // Journal of Hydraulic Research. XI 1990. 28, 6. 659–671.

Smith Stuart D., Muench Robin D., Pease Carol H. Polynyas and leads: An overview of physical processes and environment // Journal of Geophysical Research. 1990. 95, C6. 9461.

Södergren A. Helena, McDonald Adrian J., Bodeker Gregory E. An energy balance model exploration of the impacts of interactions between surface albedo, cloud cover and water vapor on polar amplification // Climate Dynamics. XI 2017. 51, 5-6. 1639–1658.

Staroszczyk Ryszard. SPH Modelling of Sea-ice Pack Dynamics // Archives of Hydro-Engineering and Environmental Mechanics. XII 2017. 64, 2. 115–137.

Staroszczyk Ryszard. Simulation of Sea-ice Thermodynamics by a Smoothed Particle Hydrodynamics Method // Archives of Hydro-Engineering and Environmental Mechanics. XII 2018. 65, 4. 277–299.

Stirling Ian. The Biological Importance of Polynyas in the Canadian Arctic // ARCTIC. I 1980. 33, 2.

Stirling Ian. The importance of polynyas, ice edges, and leads to marine mammals and birds // Journal of Marine Systems. I 1997. 10, 1-4. 9–21.

Sulsky Deborah, Schreyer Howard, Peterson Kara, Kwok Ron, Coon Max. Using the material-point method to model sea ice dynamics // Journal of Geophysical Research. II 2007. 112, C2.

Sun P.N., Colagrossi A., Marrone S., Antuono M., Zhang A.M. Multi-resolution Delta-plus-SPH with tensile instability control: Towards high Reynolds number flows // Computer Physics Communications. III 2018. 224. 63–80.

Sutherland Peter, Dumont Dany. Marginal Ice Zone Thickness and Extent due to Wave Radiation Stress // Journal of Physical Oceanography. VIII 2018. 48, 8. 1885–1901.

Swegle J.W., Hicks D.L., Attaway S.W. Smoothed Particle Hydrodynamics Stability Analysis // Journal of Computational Physics. I 1995. 116, 1. 123–134.

Tsamados M., Feltham D. L., Wilchinsky A. V. Impact of a new anisotropic rheology on simulations of Arctic sea ice // Journal of Geophysical Research: Oceans. I 2013. 118, 1. 91–107.

Tu Jiyuan, Yeoh Guan-Heng, Liu Chaoqun. Chapter 9 - Some Advanced Topics in CFD // Computational Fluid Dynamics (Third Edition). 2018. Third Edition. 369–417.

Walsh John E. The role of sea ice in climatic variability: Theories and evidencesup1/sup // Atmosphere-Ocean. IX 1983. 21, 3. 229–242.

Wang Zhilian. A coastal sea ice model with discrete parcel method. 2000. 146. Copyright - Database copyright ProQuest LLC; ProQuest does not claim copyright in the individual underlying works; Last updated - 2022-02-08.

Weiss Jérôme, Schulson Erland M., Stern Harry L. Sea ice rheology from in-situ, satellite and laboratory observations: Fracture and friction // Earth and Planetary Science Letters. III 2007. 255, 1-2. 1–8.

Wendland Holger. Piecewise polynomial, positive definite and compactly supported radial functions of minimal degree // Advances in Computational Mathematics. XII 1995. 4, 1. 389–396.

West Brendan, O'Connor Devin, Parno Matthew, Krackow Max, Polashenski Christopher. Bonded Discrete Element Simulations of Sea Ice With Non-Local Failure: Applications to Nares Strait // Journal of Advances in Modeling Earth Systems. V 2022. 14, 6.

Williams James, Tremblay L. Bruno. The dependence of energy dissipation on spatial resolution in a viscous-plastic sea-ice model // Ocean Modelling. X 2018. 130. 40–47.

Williams James, Tremblay L. Bruno, Lemieux Jean-François. The effects of plastic waves on the numerical convergence of the viscous–plastic and elastic–viscous–plastic sea-ice models // Journal of Computational Physics. VII 2017. 340. 519–533.

Yang Edward, Bui Ha H., Sterck Hans De, Nguyen Giang D., Bouazza Abdelmalek. A scalable parallel computing SPH framework for predictions of geophysical granular flows // Computers and Geotechnics. V 2020. 121. 103474.

Zhang Ningbo, Zheng Xing, Ma Qingwei. Updated Smoothed Particle Hydrodynamics for Simulating Bending and Compression Failure Progress of Ice // Water. XI 2017. 9, 11. 882.